AD_____

Award Number: DAMD17-98-1-8068

TITLE: A Novel Ultrasonic Imaging Method for Remote Palpation of Breast Tissues

PRINCIPAL INVESTIGATOR: Gregg E. Trahey, Ph.D.

CONTRACTING ORGANIZATION: Duke University
Durham, North Carolina 27708

REPORT DATE: September 2001

TYPE OF REPORT: Final

PREPARED FOR: U.S. Army Medical Research and Materiel Command
Fort Detrick, Maryland 21702-5012

DISTRIBUTION STATEMENT: Approved for Public Release;
Distribution Unlimited

The views, opinions and/or findings contained in this report are those of the author(s) and should not be construed as an official Department of the Army position, policy or decision unless so designated by other documentation.

20020329 190

# REPORT DOCUMENTATION PAGE

*Form Approved*
*OMB No. 074-0188*

Public reporting burden for this collection of information is estimated to average 1 hour per response, including the time for reviewing instructions, searching existing data sources, gathering and maintaining the data needed, and completing and reviewing this collection of information. Send comments regarding this burden estimate or any other aspect of this collection of information, including suggestions for reducing this burden to Washington Headquarters Services, Directorate for Information Operations and Reports, 1215 Jefferson Davis Highway, Suite 1204, Arlington, VA 22202-4302, and to the Office of Management and Budget, Paperwork Reduction Project (0704-0188), Washington, DC 20503

| 1. AGENCY USE ONLY (Leave blank) | 2. REPORT DATE | 3. REPORT TYPE AND DATES COVERED |
|---|---|---|
| | September 2001 | Final (1 Sep 98 - 31 Aug 01) |

**4. TITLE AND SUBTITLE**
A Novel Ultrasonic Imaging Method for Remote Palpation of Breast Tissues

**5. FUNDING NUMBERS**
DAMD17-98-1-8068

**6. AUTHOR(S)**
Gregg E. Trahey, Ph.D.

**7. PERFORMING ORGANIZATION NAME(S) AND ADDRESS(ES)**

Duke University
Durham, North Carolina 27708

E-Mail: gregg.trahey@duke.edu

**8. PERFORMING ORGANIZATION REPORT NUMBER**

**9. SPONSORING / MONITORING AGENCY NAME(S) AND ADDRESS(ES)**

U.S. Army Medical Research and Materiel Command
Fort Detrick, Maryland 21702-5012

**10. SPONSORING / MONITORING AGENCY REPORT NUMBER**

**11. SUPPLEMENTARY NOTES**

**12a. DISTRIBUTION / AVAILABILITY STATEMENT**
Approved for Public Release; Distribution Unlimited

**12b. DISTRIBUTION CODE**

**13. Abstract** ***(Maximum 200 Words)*** *(abstract should contain no proprietary or confidential information)*

A method of acoustic remote palpation, capable of imaging local variations in the mechanical properties of soft tissue is under investigation. Acoustic Radiation Force Impulse (ARFI) imaging uses focused ultrasound to apply localized radiation force to small volumes of tissue (2 $mm^3$) for short durations (less than 1 msec) and the resulting tissue displacements are mapped using ultrasonic correlation based methods. The tissue displacements are inversely proportional to the stiffness of the tissue, and thus a stiffer region of tissue exhibits smaller displacements than a more compliant region. Due to the short duration of the force application, this method provides information about the mechanical impulse response of the tissue, which reflects variations in tissue visco-elastic characteristics.

We have developed an ARFI imaging system, and performed ARFI imaging in breast tissue *in vivo*. Differences in the magnitude and the transient response of tissue displacement are correlated with tissue structures in matched B-mode images. The findings support the clinical feasibility of the method.

**14. Subject Terms (keywords previously assigned to proposal abstract or terms which apply to this award)**
1) breast cancer 2) acoustic radiation force 3) ultrasound
4) Tissue Young's modulus 5) tissue visco-elasticity

**15. NUMBER OF PAGES**
52

**16. PRICE CODE**

| 17. SECURITY CLASSIFICATION OF REPORT | 18. SECURITY CLASSIFICATION OF THIS PAGE | 19. SECURITY CLASSIFICATION OF ABSTRACT | 20. LIMITATION OF ABSTRACT |
|---|---|---|---|
| Unclassified | Unclassified | Unclassified | Unlimited |

# Contents


1 **Front Cover** 1

2 **Standard Form 298** 2

3 **Table of Contents** 3

4 **Introduction** 5

5 **Body** 5

5.1 Task 1: Modeling of Radiation Force Induced Tissue Motion . . . . . 5

5.2 Task 2: Experimental Implementation of the Method . . . . . 6

5.3 Task 3 - Analysis of Potential Tissue Heating . . . . . 8

5.4 Task 4: Pilot Clinical Study . . . . . 11

6 **Key Research Accomplishments** 14

7 **Reportable Outcomes** 15

7.1 Publications . . . . . 15

7.2 Proceedings . . . . . 15

7.3 Presentations . . . . . 15

7.4 Patent . . . . . 16

7.5 Funding . . . . . 16

8 **Conclusions and 'So What'** 16

9 **Bibliography** 17

**10 Appendices** **19**

10.1 In vitro experimental paper (JASA) . . . . . 20

10.2 In vivo clinical paper (submitted to UMB) . . . . . 31

# 4 Introduction

The early detection of breast cancer reduces patient mortality. The most common method of breast cancer detection is palpation. However, lesions that lie deep within the breast are difficult to palpate when they are small. Thus, Acoustic Radiation Force Impulse (ARFI) imaging, a method of remote palpation which may allow the detection of small lesions lying deep within the breast, is currently under investigation. In this method, focused ultrasound is used to apply localized radiation force to small volumes of tissue (2 $mm^3$) for short durations (less than 1 msec) and the resulting tissue displacements are mapped using ultrasonic correlation based methods. The tissue displacements are inversely proportional to the stiffness of the tissue, and thus a stiffer region of tissue exhibits smaller displacements than a more compliant region. Due to the short duration of the force application, this method provides information about the mechanical impulse response of the tissue, which reflects tissue visco-elastic characteristics. The research performed during the three years of support includes: finite element modeling of tissue mechanical and thermal response to ARFI imaging, experimental validation of the mechanical model, design and construction of calibrated tissue phantoms, development of real-time ARFI imaging pulse sequences (with data processing performed off-line), and a pilot clinical study of ARFI imaging in the breast.

# 5 Body

ARFI imaging is an entirely new imaging modality that provides information about the mechanical properties of tissue. Support was provided over the last three years for the purpose of developing an ARFI imaging system, and establishing the clinical feasibility of the method. This has been accomplished, and a detailed explanation of the performance of the tasks outlined in the statement of work and the associated findings follow.

## 5.1 Task 1: Modeling of Radiation Force Induced Tissue Motion

This task was completed in year 2, however the finite element models that have been developed continue to be upgraded and utilized as beam sequences are modified. Finite element mesh generation was accomplished using Hypermesh (Altair Computing Inc., Troy MI). Numerical solution of the equations of motion was accomplished using LS-DYNA3D, an explicit three-dimensional finite element code for analyzing the dynamic responses of solids (Livermore Software Technology Corporation, Livermore, CA). Initially, modeling efforts focused on determining the steady state tissue displacements associated with the application of acoustic radiation force in a single location. These models included the complex spatial distribution of the force field associated with different transducer focal configurations. It was determined that the tighter the focal configuration (i.e. the lower the F-number), the larger the resulting tissue displacement [8]. Efforts then turned to evaluation of tissue displacement in the presence/absence of a stiff, spherical inclusion (i.e. a breast lesion). These simulations demonstrated that considerably different displacement patterns are obtained in the presence/absence of a lesion [8]. The work then turned to evaluation of the displacements associated with lesions of differing size and stiffness. In all cases studied, the presence of the

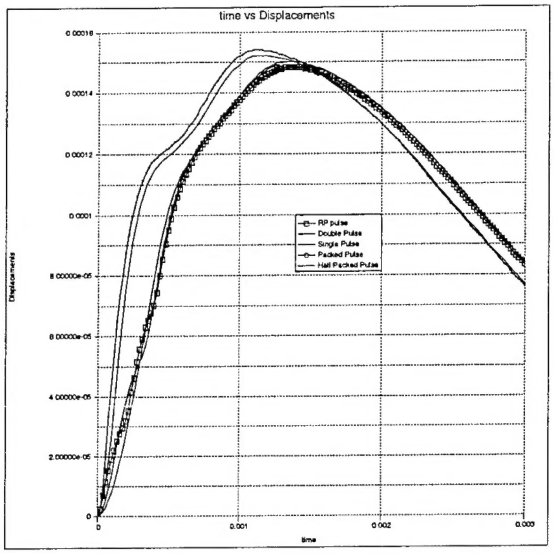


Figure 1: Plot of the displacement versus time in the center of the focal region for 5 simulated ARFI pulse sequences. All these sequences deliver the same impulse. The RP pulse is similar to that currently used for ARFI imaging (a series of three pulses, each of which are 27 microseconds long, separated by 180 msec). The packed pulse has the same magnitude as the RP pulse, except that it is constant rather than intermittent. The single pulse is a low magnitude pulse with a duration identical to the RP sequence. The double pulse consists of 2 pulses at 1/4 the magnitude of the RP pulse, and equal in duration to the RP pulse. The half-packed pulse has half the magnitude of the packed pulse and twice the duration.

lesion altered the displacement pattern, thus supporting the feasibility of the method [8].

Upon evaluation of the thermal effects of ARFI imaging (Task 3), it was determined that short duration, higher intensity radiation force application would be more effective in generating appreciable tissue displacements, while minimizing tissue heating. Therefore, the FEM model has been expanded to evaluate the dynamic response of the tissue (Fig. 1) associated with a rapid application of radiation force.

## 5.2 Task 2: Experimental Implementation of the Method

The work outlined in the Statement of Work under this task has been completed, as described below. As discussed in previous reports, instead of procuring a single phantom, we have developed a phantom fabrication facility, which allows the generation of phantoms with varying material properties. Multiple phantoms have been developed including: homogeneous phantoms, single lesion phantoms with varying lesion to tissue stiffness ratios (one of which was used to generate Fig. 8 in reference [9]), and multi-lesion phantoms which are

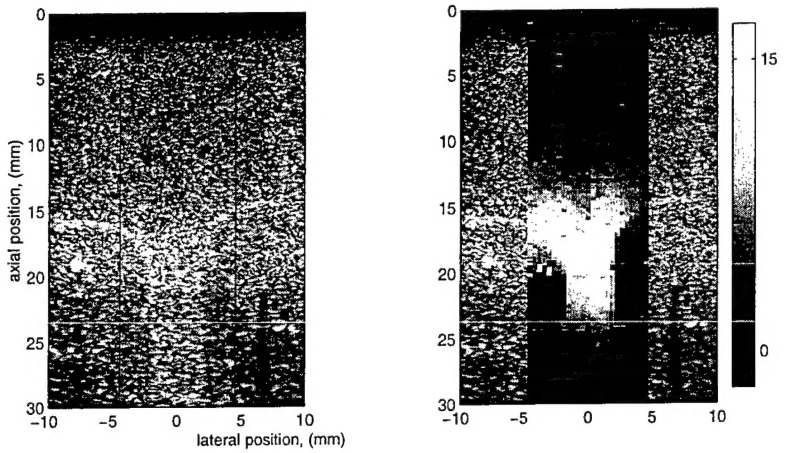


Figure 2: ARFI displacement image immediately after cessation of radiation force (right), and matched B-mode image (left) of a phantom with 2 lesions. The lesions are clearly portrayed in the ARFI image as regions of smaller displacement (i.e. darker), with higher contrast than in the B-mode image. The background medium is softer than the lesions, as evidenced by the larger displacement magnitudes. Note that the axial and lateral resolution of the images appear to be comparable.

used to evaluate the resolution of the ARFI imaging system (see Fig. 2).

Experiments were performed using our state-of-the-art Siemens Elegra diagnostic ultrasound scanners, that have been modified to allow user control of the acoustic beam sequences and provides access to the raw Radio-Frequency echo data. A Siemens 75L40 linear array was used for the experiments. Lower intensity conventional diagnostic B-mode pulses were used for tracking beams, which were interspersed with high intensity pushing beams. The intensity of the pushing and tracking beams was measured experimentally using a PVDF hydrophone in accordance with the recommended guidelines [3]. The pushing beam *in situ* intensities used for the initial experiments ranged from 3 to 80 W/cm$^2$. Initially, as with the FEM simulations, steady state displacements were achieved by firing the pushing beams for 10 milliseconds [9]. Displacements of up to 70 microns were observed in the phantoms. These experiments demonstrated that the presence of a stiff inclusion in a homogeneous background can be detected with ARFI imaging, and that the contrast in the ARFI image can be greater than that in a matched B-mode image (Figs. 9 and 10 in reference [9]). These experiments were performed in phantoms that were an order of magnitude lower in stiffness than that expected in tissue. Therefore, one conclusion from these experiments was that higher intensities were needed to generate detectable displacements *in vivo*.

This observation, in conjunction with the thermal analyses discussed in the following section, led us to modify the acoustic beam sequence for ARFI imaging. The use of higher intensities required a decrease in the application time in order to avoid heating the tissue. Therefore, the

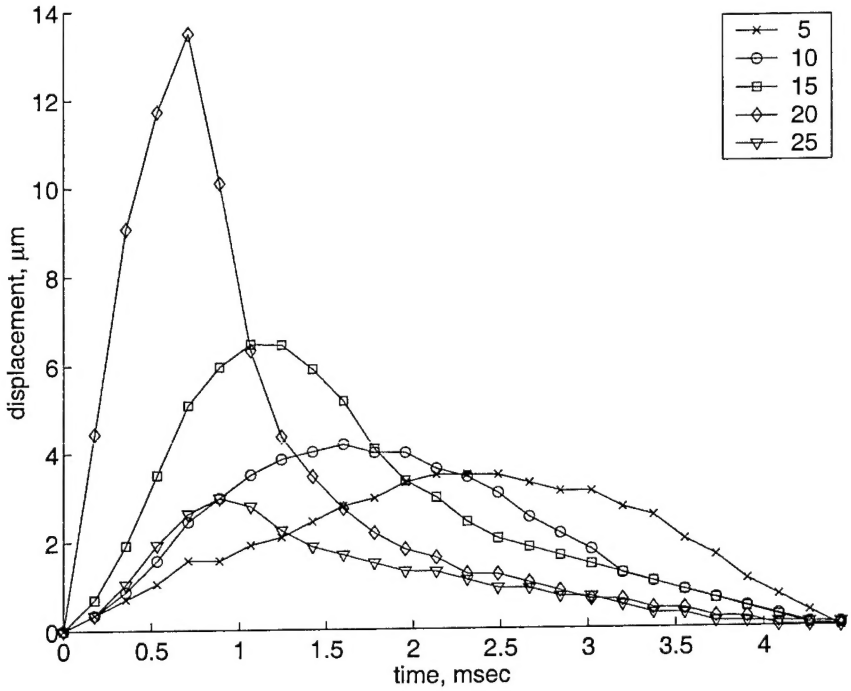


Figure 3: Displacement through time at different depths (as indicated in mm in the legend) in a homogeneous phantom. Note that propagation of the peak displacement toward and away from the focal region is apparent both as a decrease in the excitation and recovery velocities (*i.e.* the slopes of the curve during and after force application, respectively) as well as a delay in the location of the peak displacement with increasing distance from the focus (20 mm).

application time was decreased to 0.7 milliseconds, which allowed the use of *in situ* intensities of up to 1000 W/cm$^2$. The decrease in temporal application time presents an additional imaging opportunity. Now, instead of evaluating the steady state tissue displacement, we can effectively observe the mechanical impulse response of the tissue. This provides information about the visco-elastic characteristics of the tissue. As shown in Fig. 3, we can observe the displacement through time at different depths in the tissue. This allows evaluation of the excitation velocity (slope of displacement vs. time during force application), the recovery velocity (slope of displacement vs. time after force cessation), and the time it takes for the tissue to reach its to peak displacement, all of which may be useful for tissue characterization. In a phantom with two lesions and a string, it is clear that images of the different parameters allow visualization of different features in the phantom (see Fig. 4). These findings present several potential clinical opportunities for ARFI imaging.

## 5.3 Task 3 - Analysis of Potential Tissue Heating

Solution of the bio-heat transfer equation (Eqn. 1) is the accepted method for estimation of thermal increases due to ultrasonic absorption [4, 5, 11, 12, 14, 15, 6, 7, 13, 2], and is the

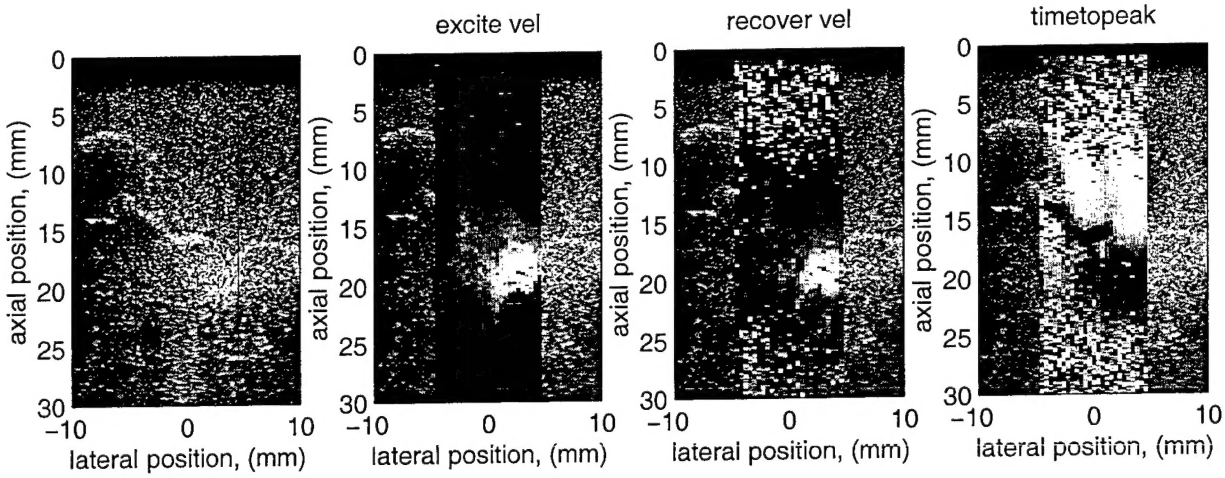


Figure 4: B-mode image, ARFI image of excitation velocity, ARFI image of the tissue recovery velocity, and ARFI image of the time it took for the tissue to reach its peak displacement in a phantom with two lesions connected by a string. Note that the upper boundary of the kidney shaped lower lesion is most clearly defined in the excitation velocity image, and that the string connecting the lesions is most clearly defined in the time to peak displacement image.

recommended method of the National Council on Radiation Protection [6, 7], the American Institute of Ultrasound in Medicine [1], and the United States FDA [3]. The bio-heat transfer equation is given below [11, 12]:

$$\frac{\partial T}{\partial t} = \kappa \nabla^2 T - \frac{T}{\tau} + \frac{q_v}{\gamma_v}, \tag{1}$$

where $T$ is the temperature, $\kappa$ is the thermal diffusivity, $\tau$ is the perfusion time constant, $q_v$ is the rate of heat production per unit volume, and $\gamma_v$ is the volume specific heat for tissue. For our application, $q_v$ represents the acoustic power absorbed by the medium, which is provided by the following equation [11, 7]:

$$q_v = 2\alpha I \tag{2}$$

where $\alpha$ is the absorption coefficient of tissue, and $I$ is the temporal average intensity of the acoustic beam that passes through a given region of tissue. Equation 2 is directly applicable for a plane wave; in addition, for focused, pulsed acoustic beams applied to absorbing tissues (as is the case for RP) it can be applied throughout the focal region of the acoustic beam [6, 7].

For simple beam geometries (*i.e.* a point source), Equation 1 can be solved analytically [11], however, for more complex beam geometries (such as those used in RP), the equation must be solved numerically [13]. Results obtained from numerical solution of equation 1 have been validated experimentally under various ultrasonic imaging conditions [15, 2]. A finite element model that numerically solves the bio-heat transfer equation as it applies to ARFI imaging has been developed, thus completing the work listed in this task. The results have been used to determine the anticipated tissue temperature increase associated with the

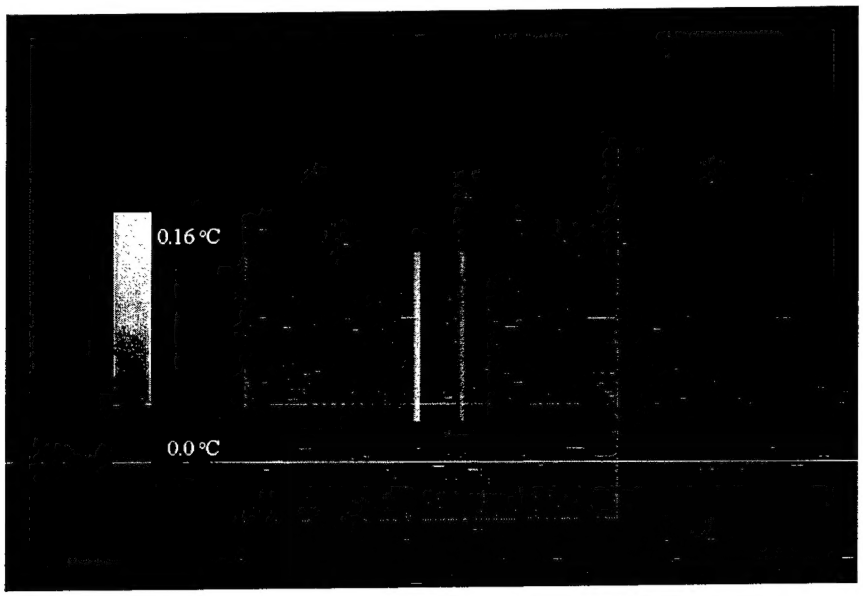


Figure 5: Thermal response of tissue to ARFI beam sequence (using only 7 pushing locations) that is currently implemented clinically. Note that there is no overlap in the heated regions from one pushing location to the next, and that the maximum temperature increase in each location is less than 0.16°C.

different beam sequences used for ARFI imaging (Fig. 5). Beam sequences are selected such that tissue temperature increases are less than 1°C.

In addition to the FEM model, a simplified analytic model has been developed that provides a worst-case estimate of the expected thermal increases. Equation 1 accounts for both the effects of conduction ($\kappa\nabla^2 T$, the removal of heat through spatial diffusion), and convection ($\frac{T}{\tau}$, the transfer of heat by blood flow or other means), both of which decrease the maximum temperature rise. Neglecting these terms allows a simple calculation of the worst-case temperature increase associated with a given acoustic beam sequence transmitted into an absorbing medium. Under these simplifying assumptions, Equation 1 becomes:

$$\frac{\partial T}{\partial t} = \frac{q_v}{\gamma_v}. \tag{3}$$

Solution of Equation 3 provides a linear relationship between the increase in temperature and the application time and intensity of the acoustic beams, as well as the absorption coefficient of the tissue:

$$T - T_o = \Delta T = \frac{q_v}{\gamma_v} t = \frac{2\alpha I}{\gamma_v} t, \tag{4}$$

where $\Delta T$ is the increase in temperature, and $t$ is the application time. Solving this equation using values that are applicable to ARFI (Table 1), we estimate the anticipated temperature rise associated with ARFI imaging in a single pushing location (Table 1).

From Figure 5 we see that the maximum temperature increase associated with ARFI imaging as it was originally proposed (i.e. longer duration applications to achieve steady state tissue

| Parameter | Units | Original Sequence | Current Sequence |
|---|---|---|---|
| I | $W/cm^2$ | 250 | 1000 |
| $t$ | seconds | 0.01 | 0.0007 |
| $\alpha^*$ | Np/cm | 0.415 | 0.415 |
| $\gamma_v$ | Joules/($cm^3$°C) | 4.2 | 4.2 |
| $\Delta T$ | °C | 0.49 | 0.14 |

Table 1: Typical values for parameters and solutions to equation 4. The 'Original Sequence' is the sequence that was fired for 10 msec in order to achieve a steady state displacement, and was used to generate the simulation results in Figure 5. The 'Current Sequence' is the sequence that is currently implemented that is fired for only 0.7 msec. *Values for $\alpha$ are typically quoted in units of dB/cm/MHz, the value provided here corresponds to an absorption coefficient of 0.5 dB/cm/MHz and an assumed center frequency of 7.2 MHz.

displacements) will be less than 0.5°C in each pushing location. Comparison of Table 1 and Figure 5 indicates that the analytic solution (Equation 4) is in agreement with the finite element simulation; although, as expected due to the simplifying assumptions, the analytic solution provides a slightly larger peak value (0.49°C vs. 0.43°C). Table 1 also indicates that the current beam sequences will result in temperature increases that are less than 0.15°C in each pushing location.

## 5.4 Task 4: Pilot Clinical Study

A pilot clinical study of ARFI imaging has been performed. In year 2 of our funding, we reported that three patients had been imaged, and that detectable displacements were observed in one of the three patients. We further reported that system modifications were required to provide more power output. In the final year of the grant, we implemented the required system power supply modifications. This allowed us to generate the new beam sequences that create *in situ* intensities of up to 1000 $W/cm^2$ for only 0.7 milliseconds in each pushing location. With the upgraded scanner, we can perform ARFI imaging in a real-time data acquisition mode that allows up to 30 spatially separated pushing locations. Using this new sequence, nine patients were imaged as of September 1, 2001, bringing the total number of patients imaged during the pilot clinical study to 12.

In addition to imaging breast tissue, we have imaged other regions of the body in healthy volunteers in order to demonstrate clinical viability of the method and to evaluate different beam sequences. The results of these studies have been submitted for publication [10]. In general, variations in displacement magnitude in the ARFI images are highly correlated with structures in the matched B-mode images (Fig. 6). Peak tissue displacements ranged from 5 to 13 microns. In some cases, brighter structures in the B-mode images appear softer than the surrounding tissue (*i.e.* they move farther), and in some cases they appear stiffer. This indicates that, as expected, tissue brightness in a B-mode image is not directly related to tissue stiffness.

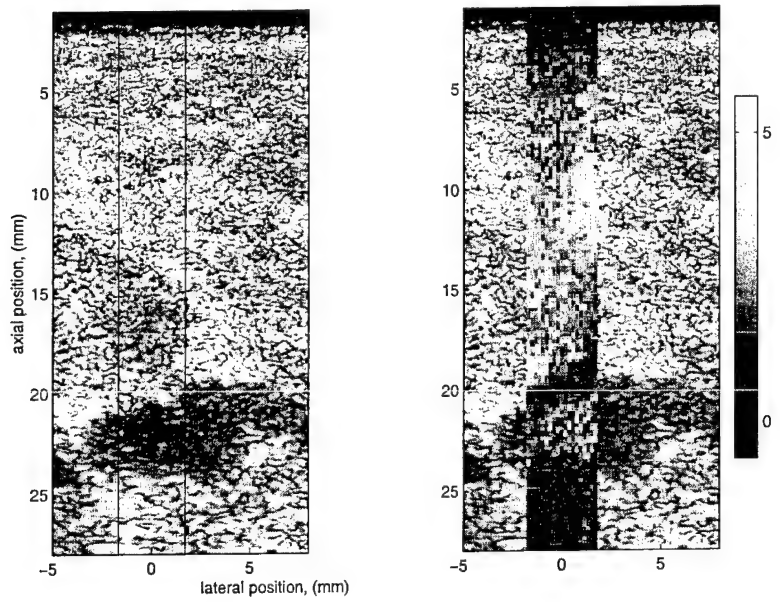


Figure 6: ARFI image of tissue displacement at 0.8 msec (right), and matched B-mode image (left) in an *in vivo* female breast. The transducer is located at the top of the images, and the colorbar scale is microns. There is a lesion located on the right side of the images between 20 and 25 mm that is evident as a darker region of tissue in the B-mode image (white arrow). This lesion was palpable, and upon aspiration was determined to be an infected lymph node. In the ARFI image, the lesion boundary appears stiffer than its interior and the tissue above it (*i.e.* it exhibits smaller displacements). In addition, the oval structure in the B-mode image immediately above and to the left of the lesion (black arrow) appears to be outlined as a softer region of tissue than its surroundings in the ARFI image.

Different tissues exhibit different transient responses to the ARFI pushing beams. This finding led us to develop new methods for displaying the ARFI data. In addition to peak displacement, images of recovery velocity and the time it took for the tissue to reach its peak displacement were generated. For example, Fig. 7 is an image of the recovery velocity that was observed in one of the patients. Note that some darker regions in the ARFI images (indicated by black arrows) are directly correlated with the microcalcifications that are present in the matched ultrasound image (indicated by white arrows). This finding is exciting in that ARFI imaging may present a method for identifying microcalcifications without exposing the patient to ionizing radiation.

An interesting finding in all of the clinical data is that the region of tissue over which radiation force is applied appears to be much larger than that predicted by our simulations, and demonstrated in our phantom experiments. This is likely due to differences in absorption and nonlinearity of tissue as compared to the phantoms, a hypothesis which is currently under investigation.

We have received NIH funding to perform an expanded clinical study of ARFI imaging,

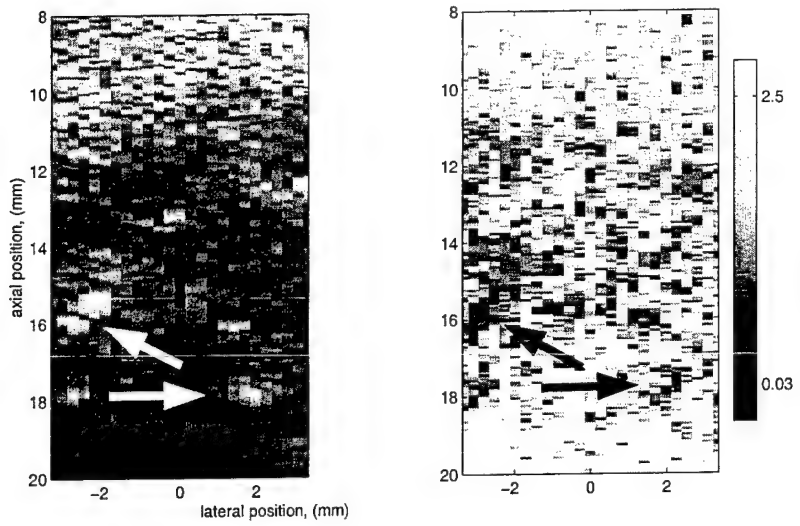


Figure 7: ARFI image of tissue recovery velocity (right), and matched B-mode image (left) in an *in vivo* female breast. The transducer is located at the top of the images, and the colorbar scale is mm/sec. Although the ARFI image is very noisy, it can be seen that the data corresponding to microcalcifications exhibits a much slower recovery velocity than most of the other tissue.

largely due to the work accomplished under this grant, therefore, although only 12 of the 20 proposed patients were imaged under this funding mechanism, we consider Task 4 to be successfully completed.

# 6 Key Research Accomplishments

- Developed and experimentally validated a finite element model of radiation force induced tissue motion.
- Determined that *in situ* intensities on the order of 1000 W/cm$^2$ were required for generation of detectable tissue displacements *in vivo*
- Determined that the required application time for such intensities is less than 1 millisecond.
- Designed and validated an analytic model that indicates that the application of these intensities for these durations will not heat the tissue more than 1°C.
- Determined that the new, short duration force application allows observation of the mechanical impulse response of the tissue, which provides information about the viscoelastic characteristics of the tissue.
- **Created the first *in vivo* ARFI images.**
- Determined that there is good correlation between the structures in the ARFI and matched B-mode images.
- Determined that the resolution of ARFI images is comparable to that of conventional ultrasound.
- Determined that *in vivo* the axial extent of the region of radiation force application is much greater than in phantoms or simulations.

# 7 Reportable Outcomes

## 7.1 Publications

Nightingale KR, Soo MS, Nightingale RW, Trahey GE. "Acoustic radiation force impulse imaging: *in vivo* demonstration of clinical feasibility", *Ultrasound Med. Biol.*, in submission.

Palmeri ML, Nightingale RW, Trahey GE, Nightingale KR. "A finite element model of the thermal effects associated with acoustic radiation force impulse imaging", *IEEE UFFC*, in preparation.

Nightingale KR, Palmeri ML, Nightingale RW, Trahey GE."On the feasibility of remote palpation using acoustic radiation force", *JASA*, 110(1):625-634, 2001.

Nightingale KR, Nightingale RW, Palmeri ML, Trahey GE."A finite element model of remote palpation of breast lesions using ultrasonic radiation force: factors affecting tissue displacement", *Ultrasonic Imaging*, 22(1):35-54, 2000.

## 7.2 Proceedings

Nightingale KR, Soo MS, Nightingale RW, and Trahey GE. "Investigation of Real-time Remote Palpation Imaging", *Proceedings of the 2001 SPIE Conference on Medical Imaging*, 2001.

Nightingale KR, Palmeri ML, Nightingale RW, Trahey GE. "Acoustic Remote Palpation: initial *in vivo* results", *Proceedings of 2000 IEEE Ultrasonics Symposium*, 2000.

Nightingale KR, Nightingale RW, Palmeri ML, Trahey GE. "Finite Element Analysis of Radiation Force Induced Tissue Motion with Experimental Validation", *Proceedings of 1999 IEEE Ultrasonics Symposium*, 1999.

## 7.3 Presentations

Nightingale KR, "Remote Palpation using Acoustic Radiation Force: Implementation and Clinical Applications", Invited Lecture, Allerton Conference on Elasticity Imaging, Montecello, IL, May 31, 2001.

"Acoustic Remote Palpation: Initial Simulation and Experimental Results", DOD BCRP Era of Hope meeting in Atlanta, GA, June 8-11,2000.

"An Experimental Investigation of the Required Acoustic Power for In Vivo Implementation of Radiation Force Based Imaging", Twenty-fifth International Symposium on Ultrasonic

Imaging and Tissue Characterization in Arlington, VA, May 24, 2000.

"Acoustic Radiation Force Induced Motion to Characterize Variations in Tissue Stiffness: Initial Experimental Results", 2000 Annual Convention of the American Institute of Ultrasound in Medicine, San Francisco, CA, April 5, 2000.

"The use of Radiation Force Induced Tissue Displacements to Image Stiffness: a Feasibility Study", Twenty-third International Symposium on Ultrasonic Imaging and Tissue Characterization in Arlington, VA, May 28, 1998.

### 7.4 Patent

"Method and Apparatus for the Identification and Characterization of Variations in Tissue Stiffness", Nightingale KR, Palmeri ML, Nightingale RW, Trahey GE. Provisional Patent Application filed April 5, 2000; Regular Patent Application filed September 18, 2000.

### 7.5 Funding

Whitaker Foundation: RG-00-0272 (Nightingale, K.), 9/01 - 8/04, $234,335, "A Radiation Force Based Ultrasonic Imaging System for the Early Detection of Breast Cancer".

NIH: 1 R01 CA92183-01 (Nightingale, K.), 9/01 - 8/05, $830,000, "Remote Palpation Imaging in the Breast".

## 8 Conclusions and 'So What'

The clinical implications of the results obtained over the duration of this support are promising. An entirely new imaging modality has been investigated that shows considerable clinical potential. ARFI images provide information about the local mechanical impulse response of tissue. Using a single transducer on a modified diagnostic scanner, ARFI data can now be collected in real-time, and processed offline. The method has been shown to be clinically feasible and safe. Structures apparent in the resulting ARFI images portray good correlation with structures in the matched B-mode images. ARFI images have comparable resolution to conventional B-mode images. Several methods of display of the ARFI data have been developed, and this continues to be an area of investigation. Movies of the ARFI data, showing displacement through time in the image plane are available at: http://www.duke.edu/ krn/research/radforce.html. Finally, two grants have been funded as a result of this work, allowing the continuation and expansion of this project.

# 9 Bibliography

## References


[1] AIUM Bioeffects Committee. Bioeffects considerations for the safety of diagnostic ultrasound. *J. Ultrasound Med.*, 7(9, Supplement), 1988.

[2] Damianou C. and K. Hynynen. Focal spacing and near-field heating during pulsed high temperature ultrasound therapy. *Ultrasound Med. Biol.*, 19:777–787, 1993.

[3] Center for Devices and Radiological Health (CDRH). 510(k) guide for measuring and reporting acoustic output of diagnostic ultrasound medical devices. *U S Dept of Health and Human Services 1985, Rev. 1993,*, December 1994.

[4] R.C. Eberhart, A. Shitzer, and E.J. Hernandez. Thermal dilution methods: Estimation of tissue blood flow and metabolism. *Ann. NY Acad. Sci.*, 335:107–132, 1980.

[5] L. Filipczynski and J. Wojcik. Estimation of transient temperature elevation in lithotripsy and in ultrasonography. *Ultrasound Med. Biol.*, 17:715–721, 1991.

[6] NCRP. *Report No. 74: Biological Effects of Ultrasound: Mechanisms and Clinical Implications.* National Council on Radiation Protection and Measurements, NCRP Publications, Bethesda, MD 20814, 1983.

[7] NCRP. *Report No. 113: Exposure Criteria for Medical Diagnostic Ultrasound: I. Criteria Based on Thermal Mechanisms.* National Council on Radiation Protection and Measurements, NCRP Publications, Bethesda, MD 20814, 1992.

[8] K.R. Nightingale, R.W. Nightingale, M.L. Palmeri, and G.E. Trahey. A finite element model of remote palpation of breast lesions using radiation force: Factors affecting tissue displacement. *Ultrasonic Imaging*, 22(1):35–54, 2000.

[9] K.R. Nightingale, M.L. Palmeri, R.W. Nightingale, and G.E. Trahey. On the feasibility of remote palpation using acoustic radiation force. *J. Acoust. Soc. Am.*, 110(1):625–634, 2001.

[10] K.R. Nightingale, M.S. Soo, R.W. Nightingale, and G.E. Trahey. Acoustic radiation force impulse imaging: In vivo demonstration of clinical feasibility. *Ultrasound Med. Biol.*, in preparation.

[11] W.L.M. Nyborg. Solutions of the bio-heat transfer equation. *Phys. Med. Biol.*, 33:785–792, 1988.

[12] H.H. Pennes. Analysis of tissue and arterial blood temperatures in the resting human forearm. *J. Appl. Physiol.*, 1:93–122, 1948.

[13] K. Thomenius. Thermal dosimetry models for diagnostic ultrasound. In *Proceedings of the 1990 Ultrasonics Symposium*, pages 1399–1408, 1990.

[14] J. Wu and G. Du. Temperature elevation generated by a focused gaussian beam of ultrasound. *Ultrasound Med. Biol.*, 16:489–498, 1990.

[15] J. Wu and W.L. Nyborg. Temperature rise generated by a focused gaussian beam in a two-layer medium. *Ultrasound Med. Biol.*, 18:293–302, 1992.

# 10 Appendices

## 10.1 In vitro experimental paper (JASA)

# On the feasibility of remote palpation using acoustic radiation force

Kathryn R. Nightingale,[a] Mark L. Palmeri, Roger W. Nightingale, and Gregg E. Trahey
*Department of Biomedical Engineering, Duke University, Box 90281, Durham, North Carolina 27708*

(Received 13 October 2000; revised 13 October 2000; accepted 11 April 2001)

A method of acoustic remote palpation, capable of imaging local variations in the mechanical properties of tissue, is under investigation. In this method, focused ultrasound is used to apply localized (on the order of 2 $mm^3$) radiation force within tissue, and the resulting tissue displacements are mapped using ultrasonic correlation based methods. The tissue displacements are inversely proportional to the stiffness of the tissue, and thus a stiffer region of tissue exhibits smaller displacements than a more compliant region. In this paper, the feasibility of remote palpation is demonstrated experimentally using breast tissue phantoms with spherical lesion inclusions, and *in vitro* liver samples. A single diagnostic transducer and modified ultrasonic imaging system are used to perform remote palpation. The displacement images are directly correlated to local variations in tissue stiffness with higher contrast than the corresponding B-mode images. Relationships between acoustic beam parameters, lesion characteristics and radiation force induced tissue displacement patterns are investigated and discussed. The results show promise for the clinical implementation of remote palpation. © *2001 Acoustical Society of America.* [DOI: 10.1121/1.1378344]

PACS numbers: 43.80.Qf, 43.80.Sh, 43.80.Vj [FD]

## I. INTRODUCTION

### A. The remote palpation method

It is hypothesized that an acoustic radiation force can be used to generate localized tissue displacements, and that these displacements will be directly correlated with localized variations in tissue stiffness. It is further hypothesized that this can be accomplished using a single transducer on a diagnostic ultrasound scanner to both generate the radiation force and detect the resulting displacements. These hypotheses form the basis for a new imaging method called remote palpation. In this method, acoustic radiation force is used to generate localized displacements in tissue. These displacements are measured using ultrasonic correlation based methods. The magnitude of the tissue displacement is inversely proportional to the local stiffness of the tissue. Radiation force induced displacement maps are generated at multiple locations, and combined to form a single image of variations in tissue stiffness throughout an extended field of view (FOV). A single transducer on a diagnostic scanner is used to both generate the high intensity "pushing" beams and track the resulting tissue displacements.

### B. Purpose

Two potential clinical applications for remote palpation are lesion detection and characterization, and the identification and characterization of atherosclerosis. In this paper we focus on the former, as it pertains to the early detection of breast cancer, which has been shown to significantly improve patient survival. Existing methods of breast cancer detection include screening mammography and palpation, either by patient self-examination or clinical breast exam. Palpation relies on the manual detection of differences in tissue stiffness between breast lesions and normal breast tissue. The success of palpation is due to the fact that the elastic modulus (or Young's modulus) of breast lesions is often an order of magnitude greater than that of normal breast tissue,[1,2] i.e., breast lesions feel "hard" or "lumpy" as compared to normal breast tissue.

Differences in Young's moduli are the basis for the investigation of imaging modalities that provide information about the stiffness of tissue. Traditionally, these have fallen into two categories: (1) Sonoelasticity, in which low frequency shear wave propagation is imaged using Doppler or magnetic resonance methods. Estimates of the elastic modulus of the tissue are based upon this information.[3–7] (2) Elastography, in which local variations in tissue strain are determined by measuring local displacements that occur during global tissue compression. Reconstruction methods are used to determine the elastic modulii associated with the measured strain fields.[1,8–11] Remote palpation is similar to elastography, which has demonstrated some success in the detection of malignant breast lesions,[12] however it has several potential advantages. These include the very localized application of radiation force (as opposed to global external compression), the decrease in maximum tissue strain required for lesion visualization, and the potential for real-time implementation without the need for external compression fixtures.

## II. BACKGROUND

### A. Acoustic radiation force

Acoustic radiation force is a unidirectional force that is applied to absorbing or reflecting targets in the propagation path of an acoustic wave. This phenomenon is caused by a transfer of momentum from the acoustic wave to the propa-

[a]Electronic mail: kathy.nightingale@duke.edu

 0001-4966/2001/110(1)/625/10/$18.00 © 2001 Acoustical Society of America 

gation medium. The contribution of absorption is in the direction of wave propagation, whereas the contribution of scattering is dependent upon the angular scattering properties of the target. In the event that the target is both absorbing and has a scatterer that acts as a reflector with an axis of symmetry perpendicular to the direction of wave propagation (e.g., the reflecting target is spherical), the radiation force is entirely in the direction of wave propagation. In this situation, the radiation force is given by[13]

$$F=\left(\Pi_a+\Pi_s-\int \gamma\cos\theta r\,dr\,d\theta\right)\langle E\rangle, \tag{1}$$

where $\Pi_a$ is the total power absorbed by the target, $\Pi_s$ is the total power scattered by the target, $\gamma$ is the magnitude of the scattered intensity, $\theta$ is the scattering angle, $r\,dr\,d\theta$ is an area element of the projection of the target onto the axial/lateral plane, and $\langle E\rangle$ is the temporal average energy density of the propagating acoustic wave.

If there is no absorption, and the target is perfectly reflecting (i.e., $\theta=180°$), the integral term becomes $-\Pi_s$ and the total radiation force is $\{2\Pi_s\langle E\rangle\}$. The factor of 2 can be intuitively explained by the fact that the target stops the wave from propagating, and reflects it in the opposite direction.[14] If the target is a Rayleigh scatterer (i.e., its diameter is much smaller than a wavelength), scattering occurs in all directions equally, and the integral term is zero. Thus the total radiation force on the scatterer is $\{(\Pi_a+\Pi_s)\langle E\rangle\}$.

For a tissue model comprised of a collection of Rayleigh scatterers, one can sum the contribution of the radiation force from each scatterer to determine the total force due to scattering. However, in tissue, the majority of the attenuation of an acoustic wave is due to absorption,[15] thus the contribution to the radiation force by scattering in soft tissue can, in general, be neglected. Equation (1) then becomes

$$F=\Pi_a\langle E\rangle. \tag{2}$$

Assuming plane wave propagation, the radiation force applied to tissue is thus[14,16–18]

$$F=\frac{2\alpha I}{c}, \tag{3}$$

where $F$ (which is in the form of a body force, or force per unit volume) is the acoustic radiation force [kg/(s$^2$ cm$^2$)], or [dynes/(1000 cm$^3$)], $c$ (m/s) is the speed of sound in the medium, $\alpha$ (m$^{-1}$) is the absorption coefficient of the tissue, and $I$ (W/cm$^2$) is the temporal average intensity of the acoustic beam at a given point in the tissue. For a focused acoustic beam propagating through soft tissue, the "target" is the tissue, and the force is applied throughout the focal region of the acoustic beam.

A phenomenon that is not modeled by Eq. (3) is the enhancement of radiation force generated by nonlinear propagation of an acoustic wave.[18–21] For the same temporal average intensity, a wave with higher pressure amplitude and shorter pulse duration generates a larger radiation force than does a lower amplitude, longer duration wave. This is due to the higher order harmonics generated by nonlinear propagation, which result in an increase in absorption.[18–21] Nonlinear propagation also narrows the transmit beam and shifts the intensity field of a focused acoustic beam.[20] Nonlinearly enhanced increases in radiation force by a factor of 2.6 have been observed in breast applications *in vivo*.[22]

The potential applications of acoustic radiation force in diagnostic imaging have heretofore been widely ignored, primarily because the available energy from diagnostic ultrasound systems was low. However, advances in transducer and system design in recent years have resulted in considerable increases in the maximum possible acoustic energy output from these systems. This has sparked a renewed interest by several laboratories in the potential applications of acoustic radiation force. Our laboratory demonstrated the use of acoustic radiation force to induce acoustic streaming in cyst fluid, and thus differentiate fluid-filled from solid breast lesions *in vivo*.[22,23] Several authors have proposed the use of acoustic radiation force to remotely characterize the mechanical properties of tissue.[19,24–27] One application involves the use of a radiation force field oscillating at the beat frequency of two confocal transducers to vibrate an object; the vibrations are detected by a hydrophone, and are used to generate an image.[27] In another application, acoustic radiation force is used to displace tissue, and the speed of the shear waves generated immediately after force removal is monitored to characterize variations in tissue Young's modulus.[19] In yet another application, acoustic radiation force is used to manipulate the vitreous humor of the eye.[24]

### B. Tissue response to radiation force

Remote palpation applies localized forces to tissue, which can be described for idealized cases by elasticity theory. For an infinitely small distributed force volume, the strain field can be derived from the analytic solution for a point load in an infinite elastic solid:[28]

$$\epsilon_z=\frac{-(P\,z\,(1+\nu)\,(4\,z^2\,(-1+\nu)+r^2\,(-1+4\,\nu)))}{8\,E\,\pi\,(r^2+z^2)^{5/2}\,(-1+\nu)},$$

$$\epsilon_r=\frac{-(P\,z\,(-2\,r^2+z^2)\,(1+\nu))}{8\,E\,\pi\,(r^2+z^2)^{5/2}\,(-1+\nu)}, \tag{4}$$

$$\epsilon_\theta=\frac{-(P\,z\,(1+\nu))}{8\,E\,\pi\,(r^2+z^2)^{3/2}\,(-1+\nu)},$$

where $\epsilon_{z,r,\theta}$ are the 3 dimensional normal strains. The variable $z$ is the axial distance along the line-of-action of the applied force, $P$ is the magnitude of the applied force, $r$ is the radial distance from the point of applied force, $E$ is the Young's modulus of the material, and $\nu$ is Poisson's ratio. The displacement of the material in the direction of the applied force is obtained by integration of $\epsilon_z$:[28]

$$w=\frac{P\,(1+\nu)\,(4\,z^2\,(-1+\nu)+r^2\,(-3+4\,\nu))}{8\,E\,\pi\,(r^2+z^2)^{3/2}\,(-1+\nu)}. \tag{5}$$

Solving these equations for a magnitude of force similar to that used in RP [i.e., $P=1$ dyne, $\nu=0.49$, $E=30{,}000$ dynes/cm$^2$ (3.0 kPa)] gives an estimate of the size of the associated displacement and strain fields. The solution indicates that the spatial extent of the axial strain field is very

small, with strains decreasing to a negligible amount at a distance of 0.2 mm from the loading point (Fig. 1). Strains in the radial and circumferential directions are even smaller. This implies that lesions that are separated by more than 0.4 mm can be differentiated when excited with point loads at a 0.2 mm spacing.

### C. High intensity acoustic beams

Potential risks associated with remote palpation arise from the fact that high intensity acoustic pulses are utilized. The FDA provides two indices to monitor the safety of diagnostic ultrasound. The mechanical index (MI) is indicative of the potential for cavitation, and the thermal index (TI) is indicative of the potential temperature rise. The high intensity pulses used in remote palpation do not exceed the MI limit of 1.9;[29] cavitation is not anticipated due to the use of relatively high frequencies (7 to 14 MHz). It is not anticipated that the TI will exceed 6, which is the limit above which the FDA requires special provisions for approval of use. Finite element models of the heating associated with the high intensity beams used for remote palpation indicate that the temperature rise will be less than 1 °C,[30] which would correspond to a TI of 1.

Throughout this paper, the derated (or *in situ* estimated) spatial peak temporal average intensity for the different acoustic beams is provided in order to calibrate the reader. The FDA currently limits the spatial peak temporal average intensity ($I_{spta.3}$) to 0.72 W/cm$^2$ *in situ*,[29] which is intended as an indirect indicator of potential tissue heating. However, this limit was determined assuming an indefinite application time. Short duration, high intensity acoustic pulses as are used in remote palpation (i.e., less than 10 milliseconds) were not foreseen in the development of this FDA limit, and thus the TI and/or temperature increase estimates provide a more appropriate indication of the potential for thermal effects.

### D. Goals

The goals of the work presented herein are the following: first, to experimentally demonstrate the feasibility of remote palpation imaging; second, to determine whether the displacement images generated during remote palpation imaging are directly correlated with variations in tissue stiffness; and third, to determine whether a single transducer on a diagnostic scanner can be used to perform remote palpation imaging.

## III. METHODS

Experiments were performed with a Siemens Elegra scanner (Siemens Medical Systems, Ultrasound Group, Issaquah, WA), that has been modified to allow user control of the acoustic beam sequences and intensities, as well as providing access to the raw radio-frequency (RF) data. A Siemens 75L40 linear array was used for these experiments. Figure 1 provides a schematic of a typical linear array, and defines the different dimensions discussed below. The 75L40 array consists of 194 elements, each of which are 5 mm tall and approximately 0.2 mm wide, with a center frequency of

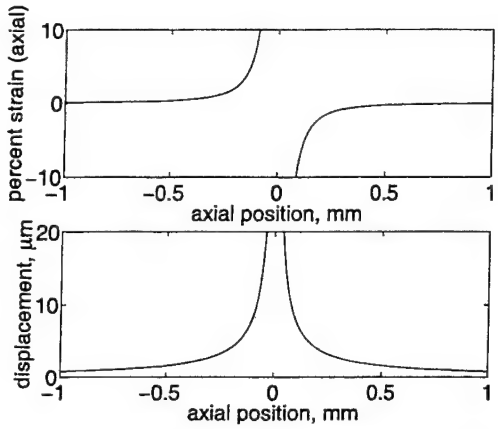


FIG. 1. Percent axial strain (top) and associated axial displacement (bottom) resulting from the application of a point load with a force magnitude similar to that used for remote palpation (i.e., $P=1$ dyne), in an elastic medium with material properties consistent with those of tissue [i.e., $\nu=0.49$, $E=30{,}000$ dynes/cm$^2$ (3.0 kPa)].[28] Note that the axial extent of both fields has decreased to an insignificant amount within 0.2 mm of the location of force application (0 mm).

7.2 MHz. The number of active elements can be selected electronically to adjust the lateral transmit aperture width. There is a fixed-focus acoustic lens on each element that focuses in the elevation dimension. Lateral focusing is accomplished electronically by applying the appropriate delays to each active element (Fig. 2). The interrogation of different spatial locations is accomplished by using different subapertures (or groups of elements) within the array. In all of these experiments, the lateral aperture was considerably larger than the elevation aperture. This resulted in an asymmetric focal region that was more tightly focused in the lateral dimension than in the elevation dimension (in contrast to a piston, which has an axi-symmetric focal region).

The tracking beams were standard diagnostic B-mode pulses (i.e., single cycle pulses, F/1 focal configuration, apodized, $I_{spta}<0.1$ W/cm$^2$, MI$\sim$0.4), and they were fired using PRFs ranging from 3 to 5 kHz.

The pulse length, transmit voltage, and transmit F-number (i.e., number of active transmit elements) of the pushing beams were varied in the experiments. The pulse lengths ranged from 0.8 to 5.8 $\mu$s, the transmit voltages ranged from 30 to 140 V (in contrast to 20 V for the tracking beams), the F-numbers ranged from F/1 to F/3, the pulse repetition frequencies (PRFs) were varied from 3 to 5 kHz,

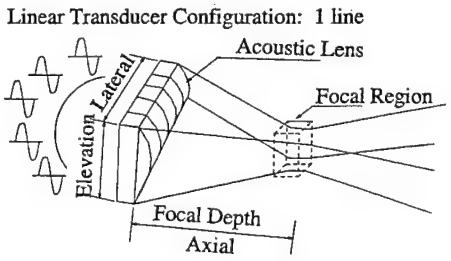


FIG. 2. Linear transducer configuration. Note that there is only 1 row of elements, and each element is much taller (elevation dimension) than it is wide (lateral dimension). There is an acoustic lens that focuses in the elevation dimension, and electronic delays are used to focus in the lateral dimension. Thus, the focal point can be varied in the lateral dimension (as was done in Fig. 5), whereas the elevation focal point is fixed.

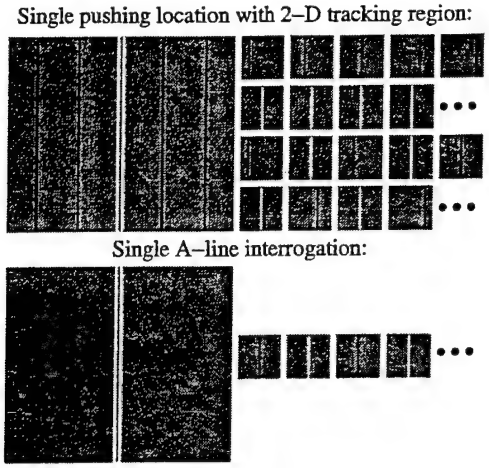


FIG. 3. Schematic of the beam sequences for the different experiments. The black lines indicate tracking lines, and the white lines indicate pushing lines. The larger image on the left presents the spatial relationship of all of the lines. The smaller images on the right indicate the line firing sequences, in order from left to right. Top: single pushing location with 2-D (B-mode) tracking region. For brevity, this schematic shows only 5 spatially separated tracking lines. The different spatial locations are interrogated by using different sub-apertures (or groups of elements) in the array. Bottom: single A-line interrogation with alternating track and push lines.

and they were not apodized. The associated *in situ* temporal average intensities ranged from 2.4 to 140 W/cm$^2$, which were applied for not more than 50 milliseconds. There was no interference between echoes from the pushing and tracking beams due to the low duty cycle of the pushing beams (1 to 3%).

Several beam sequences were designed to investigate the temporal and spatial response of the phantoms. The experiments are divided into three groups: single pushing location with a two-dimensional (2-D) tracking region, single A-line interrogation, and multiple pushing locations.

### A. Single pushing location with 2-D tracking region

For these experiments, the transducer was held in a stationary location. The pulse sequence was designed to transmit a series of 13 spatially distributed tracking beams (i.e., B-mode interrogation using 13 laterally spaced lines, Fig. 3, top) at a PRF of 3584 Hz. This was followed by 10 milliseconds of pushing beams fired at a PRF of 3584 Hz along a single line of flight in the center of the tracking beams, followed by another series of tracking beams interspersed with pushing beams (every other beam; see Fig. 3). The spacing of the tracking beams was 0.7 mm. This sequence was repeated for 50 milliseconds. The raw RF data were stored for off-line processing.

### B. Single A-line interrogation

This sequence was designed to fire all of the tracking beams in the same spatial location as the pushing beams (i.e., A-line interrogation, Fig. 3, bottom). The pulse repetition frequency (PRF) for these experiments was 10240 Hz. Every other beam was a tracking beam, thus the PRF for the tracking beams was 5120 Hz. The PRF of the pushing beams was varied by firing either every pushing pulse (PRF 5120 Hz, as shown in Fig. 3, bottom), every fourth pushing pulse (PRF 1280 Hz), every fifth pushing pulse (PRF 1024 Hz), or every sixth pushing pulse (PRF 853 Hz). The first beam fired was always a tracking beam which served as a reference for the initial position. The raw, radio-frequency (RF) data were stored and processed off-line.

### C. Multiple pushing locations with 2-D tracking regions

These sequences were the same as those described in Sec. III A, however only 11 tracking lines were utilized for each pushing location (instead of 13), and these lines were spaced at 0.09 mm. This resulted in datasets from each pushing location covering $\pm 0.5$ mm laterally. Multiple pushing locations were interrogated by connecting the transducer to an automated translation stage, and translating the transducer to interrogate different regions of tissue (using the same acoustic beam parameters and sequences at each location). These experiments were performed on two different phantoms, each with an 8 mm diameter lesion located 1.0 cm from the surface of the phantom. The phantoms were submerged in a liquid slurry phantom material, that was created by blending a homogeneous phantom. This was done in order to achieve the same absorption and attenuation of the beam for each axial transducer position, without applying compression to the phantom itself. The pushing point locations spanned 11 mm laterally, and 9 mm axially with 1 mm spacing in both dimensions (Fig. 8 top). The raw RF data from each pushing location were stored for off-line processing.

### D. Data processing

The summed RF echo data is 16 bit data, acquired from the Elegra scanner at a sampling rate of 36 MHz. The data is up-sampled to 1.8 GHz, thus given an assumed acoustic velocity of 1540 m/s the minimum measured displacement is 0.4 microns. Off-line data processing was accomplished by performing 1-D cross-correlation in the axial dimension between the up-sampled sequentially acquired tracking lines.[31,9] Each tracking line was divided into a series of search regions (0.7 mm in length), and the location of the peak in the cross-correlation function between a kernel in the first tracking line (0.5 mm in length) and the corresponding search region in the next tracking line was used to estimate the axial tissue displacement in that region. No overlap of the search regions was used. One-wavelength translations were removed and all displacements associated with a correlation coefficient greater than 0.99 were considered valid.

### E. Intensity measurements

Pressure and intensity calibration measurements were made in accordance with the guidelines provided by the American Institute of Ultrasound in Medicine.[32] These measurements are made complicated at higher transmit voltages due to acoustic saturation.[33] Saturation occurs at lower pressures in water than it does in phantoms and tissue, thus accurate measurement of the intensities and pressures used for the highest transmit voltages was not possible. However, the relationship between the acoustic radiation force and the re-

TABLE I. Phantom fabrication recipes for 300 milliliters of solution (Ref. 34).

| | Gelatin (g) | Water (ml) | N-propanol (ml) | Graphite (g) | Glutaraldehyde (25% soln, ml) | E (kPa) |
|---|---|---|---|---|---|---|
| Tissue (A,B,C) | 13.0 | 230.0 | 18.0 | 18.75 | 52.0 | ~0.1 |
| Lesion | 17.0 | 222.0 | 18.0 | 18.75 | 60.0 | 0.5 |
| Tissue (D) | 20.0 | 222.0 | 18.0 | 18.75 | 60.0 | 1.6 |

sulting displacement is linear.[26] Therefore, one can obtain an estimate of the magnitude of the radiation force generated by a very high intensity acoustic beam by comparing the corresponding peak displacement obtained in the same phantom using a lower intensity, quantifiable beam. Where Eq. (3) applies, the ratio of the forces is equal to the ratio of the intensities. Thus one can obtain an estimate of the intensity in the higher energy beam under the assumption of linear propagation by evaluating the ratio of the peak displacements.

The above approach does not account for the enhancement in radiation force caused by nonlinear propagation.[18–20,22] This results in an overestimate of the intensity of the beam, due to the assumption of a single frequency and absorption coefficient in Eq. (3). Even so, this method provides a reasonable approximation of the intensities, and thus is utilized to estimate the intensities used in the experiments where actual measurements were not possible (i.e., transmit voltages of 80 V and higher).

### F. Phantom construction

Experiments were performed both in elastography phantoms, and in thawed, de-veined calf liver. The elastography phantoms were fabricated from gelatin, graphite, alcohol, water, and glutaraldehyde.[34] The lesions in the phantoms were all generated from a single batch, with a recipe corresponding to a higher Young's modulus than the background material. Table I provides the recipes for the phantoms. The calf liver was purchased frozen from the local grocery store in a vacuum-sealed package. It was thawed under water, and the experiments were performed on the same day.

### G. Phantom mechanical property characterization

Characterization of the Young's modulus of tissue and tissue-like media is very challenging. Only a few reports exist in the literature on the subject.[2,35,36] The reported values vary considerably, possibly because Krouskop *et al.* applied pre-compression while making their measurements, whereas the other groups did not;[2,35,36] the stiffness of tissue increases with compression.[2] The numbers provided here were obtained in a method consistent with those reported. This involved modeling of the test apparatus to account for boundary condition deviations from the assumed theoretical solution, and a comparison of the experimental measurements with both the theoretical model (which had inherent assumptions) and the boundary condition correction model.[34,36] A thorough description of these methods is outside of the scope of this paper. It is possible that our measurements suffer from a constant offset, however, the relative stiffnesses of the phantoms are consistent (i.e., in order from the most compliant to the most stiff: Phantom C, Phantom A, Phantom B, Lesion Material, Phantom D).

## IV. RESULTS

### A. Phantom fabrication

Phantoms A, B, and C were designed using the same recipe shown in Table I. Phantom A had an 11 mm diameter lesion, Phantoms B and C each had an 8 mm diameter lesion. Although the ingredients were the same for each of these phantoms, the background material varied in its Young's modulus slightly between batches. This is likely due to limited control of temperature fluctuations during fabrication.

The measured Young's modulus of the lesion material was 0.5 kPa. The Young's modulus of the background material in Phantoms A, B, and C was 0.07 kPa, 0.13 kPa, and 0.05, respectively. These values are approximately an order of magnitude lower than those reported for soft tissue,[35,36] however the lesion to tissue stiffness ratios (LTSR) are between 3.8 and 10, which are consistent with LTSRs reported for breast tissue.[35]

The Young's modulus of Phantom D was 1.6 kPa. Phantom D was designed without a lesion. The Young's modulus of the liver sample used for the experiments was not measured, however reported values in the literature range from 0.4 to 1.7 kPa.[36] A comparison of the steady state displacements generated with the same remote palpation imaging sequence in both Phantom D and the liver sample indicate that Phantom D was approximately 4 times more stiff than the liver sample.

### B. Single pushing location with 2-D tracking region

Figure 4(a) portrays the two-dimensional displacement profile generated in a homogeneous portion of Phantom A for an F/1 focal configuration with a lateral focal point of 20 mm, and a relatively low transmit voltage (29 V). This image was generated after 10 milliseconds of force application, and represents the tissue displacement profile (in two dimensions) resulting from a single force application. If the acoustic beam had generated a point load, one would expect a small circular displacement profile, consistent with Fig. 1. However, the focused acoustic beam used for these experiments is associated with an intensity field that is approximately the size of its focal region. The extent of the inner contour (−2 dB) shown in Fig. 4(a) is approximately the size of the intensity field of the acoustic beam (including intensity values down to −20 dB).

The derated spatial peak temporal average intensity of the pushing beams used to generate Fig. 4(a) was 2.4 W/cm$^2$,

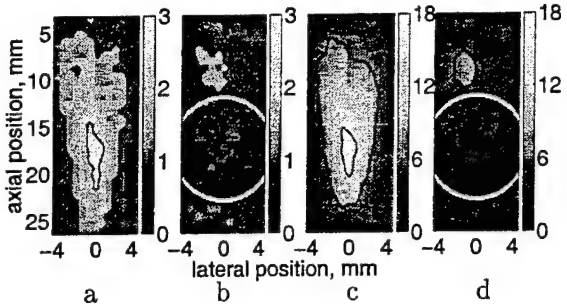


FIG. 4. Displacement maps after 10 milliseconds of force application in phantom A. For each of the images, the black contours represent levels of −2 dB and −10 dB of the peak displacement, the lateral focal point was 20 mm, the transducer was located at the top of the images, and the colorbar scale is in microns. (a) Displacement profile generated in a homogeneous region of the phantom for an F/1 focal configuration using a single pushing location and a relatively low transmit voltage (29 V), and a pulse length of 2.2 microseconds. (b) Displacement profile generated using the same beam sequence as in (a), with the pushing location centered in an 11 mm diameter lesion. The lesion boundaries are highlighted in white. Both (a) and (b) have the same colorbar scales, ranging from 0 to 3 microns. (c) Displacement profile generated in the same location as (a), also using an F/1 focal configuration but with a higher transmit voltage (80 V), and a pulse length of 0.8 microseconds. Note that the displacement profile is similar to (a), however it is shorter axially, with the peak shifted slightly closer to the transducer. This is to be expected in the presence of nonlinear propagation. (d) Displacement profile generated in the same location as (b), using the same beam sequence as in (c). Both (c) and (d) have the same colorbar scales, with displacements ranging from 0 to 18 microns.

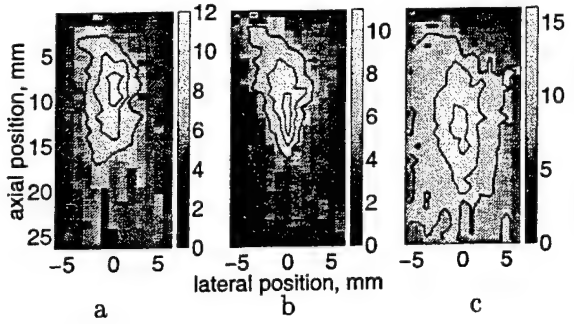


FIG. 5. Displacement maps generated in calf liver after 10 milliseconds of force application. For each of the images, the black contours represent levels of −1 dB, −3 dB, and −6 dB of the peak displacement. The units of displacement on the colorbars are microns. The transducer was located at the top of the images. A constant focal configuration of F/1 was used to generate these images, with a transmit voltage of 140 V, and a pulse length of 3.4 microseconds. (a) lateral focal point at 10 mm. (b) Lateral focal point at 15 mm. (c) Lateral focal point at 20 mm. Note that the peak in the displacement map moves with the lateral focal point, and is slightly closer to the transducer than the focal point.

and the associated radiation force, as computed using Eq. (3), was 100 dynes/cm$^3$. The maximum displacement is 2.9 microns. Figure 4(b) shows the two-dimensional displacement profile generated when the same beam sequence is focused in the center of an 11 mm diameter lesion in the same phantom. The maximum displacement is smaller than in the homogeneous case (1.4 microns), and the shape of the intensity field is not apparent in the contours of displacement.

Figure 4(c) portrays the displacement map with the pushing beams focused in the same phantom location as in Fig. 4(a), however with a much higher transmit voltage (80 V). The shape of the contours of displacement are similar to Fig. 4(a), however they are shorter axially, and the peak has shifted slightly closer to the transducer. The estimated *in situ* peak intensity ($I_{spta.3}$) of this beam is 15 W/cm$^2$ (Sec. III E). The maximum displacement is 18 microns.

Figure 4(d) was obtained using the same beam sequence as in Fig. 4(c), but focused within the lesion [in the same location as in Fig. 4(b)]. The maximum displacement is 7 microns. A comparison of image pairs a–b and c–d indicates that their differences are similar. In both image pairs, the −10 dB contours begin axially in similar locations. As predicted, the presence of the lesion decreases the peak displacement, and alters the displacement profile from the homogeneous case. In both Fig. 4(b) and Fig. 4(d) the maximum displacement is approximately half of that in the corresponding homogeneous cases [Figs. 4(a) and (c)].

Figure 5 portrays the displacement profiles generated in the calf liver sample, using different focal positions (10, 15, and 20 mm). In each case, an F/1 focal configuration was maintained (i.e., the number of active transmit elements was increased as the focal position depth increased). The estimated derated peak intensity of the beam used for the 20 mm focus is 80 W/cm$^2$ (Sec. III E). In each plot, the peak in the displacement profile occurs slightly in front of the focal position. Although the focal configuration was constant (F/1), the maximum displacement differs in each plot: 12, 11, and 16 microns, for plots a, b, and c respectively.

### C. Single A-line interrogation

Figure 6 portrays the maximum displacement through time in Phantom A. In this sequence, all of the tracking lines were fired along the same line (spatially) as the pushing lines, and the tracking and pushing lines were interspersed

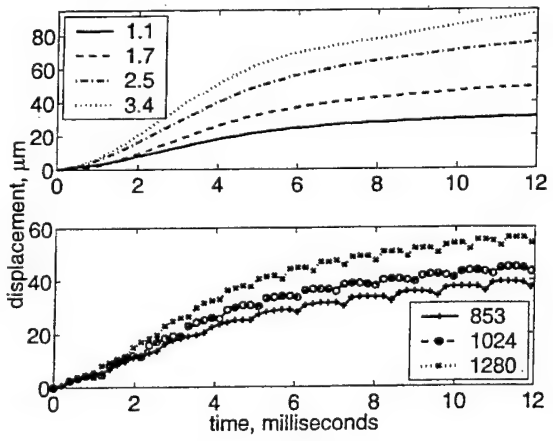


FIG. 6. Displacement through time near the position of peak displacement (17.5 mm from the transducer) in phantom A. Top: The pulse length of the pushing pulses was varied for each curve as indicated in the legend in units of microseconds, but the PRF was held constant (3584 Hz), as was the focal configuration (F/1) and transmit voltage (140 V). Note that, as expected, the steady state displacement for the 3.4 microsecond pulse is double that of the 1.7 microsecond pulse. Bottom: For each of these curves, the same pushing pulses were used (F/1 focal configuration, a pulse length of 5.8 microseconds, and a transmit voltage of 140 V) but with different pushing pulse PRFs. The frequency of the 'rectified sine wave' apparent in each of the three plots corresponds to the PRF of the high intensity beams for each experiment (as indicated in the legend, in Hz). This is due to the recovery of the tissue between pushing beams. Note that the magnitude of the recovery increases over time, with increasing mean tissue displacement.

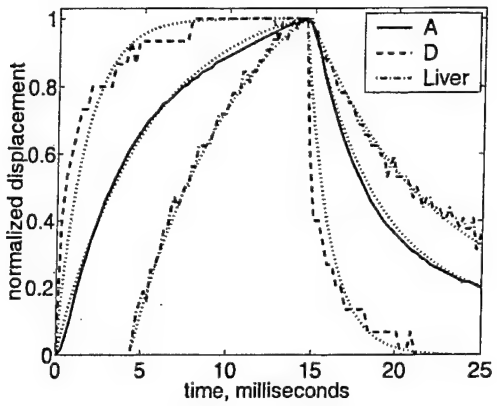


FIG. 7. Displacement over time in the focal region of the transducer for Phantoms A and D in a homogeneous portion of each phantom, as well as in the liver sample. In both Phantom A and the liver sample, the pushing pulses were 3.4 microseconds long, with an F/1 focal configuration and a transmit voltage of 140 V. In Phantom D, the pushing pulses were 5.8 microseconds long, with an F/1 focal configuration and a transmit voltage of 140 V. In all experiments the pushing pulses and tracking pulses were interspersed, and the pushing pulses were fired for a total of 52 lines, and then turned off. The PRF in the liver sample was 5120 Hz, whereas in phantoms A and D it was 3584 Hz. The time at which the pushing pulses were turned off has been aligned in these plots for ease of analysis. The dashed lines represent exponential fits to the data. The time constants for the ramp up time are 5.1, 1.6, and 6.2 milliseconds for phantoms A, D, and the liver sample, respectively. The time constants for the recovery are 4.2, 1.5, and 7.9 milliseconds for phantoms A, D, and the liver sample, respectively.

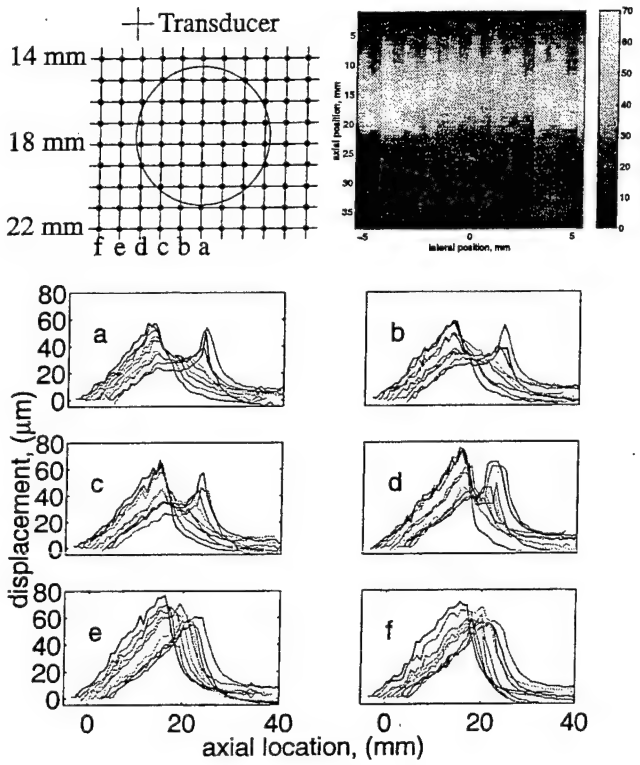


FIG. 8. Top left: Grid of pushing locations (9×11 mm, 1 mm spacing in both the axial and lateral directions) and their relationship to the lesion. Each dot at the grid intersections represents an independent pushing location focal point (and thus a different position of the translation stage and transducer). At each position, the beam sequence described in Sec. III A was fired (with line spacings as described in Sec. III C). The 2-D tracking region surrounding each pushing focal point extends across the entire ROI axially, and laterally it extends ±0.5 mm, halfway between each of the neighboring focal point positions (i.e., dots) to the left and right. Top right: Raw data from the fourth row of pushing locations (including all of the lateral tracking lines) used to generate the image shown in Fig. 9. The colorbar scale is in microns, and the transducer is located at the top of the image. Note that although the focal position of the pushing beams is at a fixed range (19 mm), the lesion is well defined from 12 to 21 mm axially. Bottom: Each subplot represents the displacement along the axis of the high intensity pushing beam for the 9 axial pushing locations at each lateral position shown on the grid above [(a)–(f)]. The transducer is at the left side of these plots. The lesion is clearly apparent as a "dip" in the displacement profiles in lines a-d, and the width of the "dip" is consistent with the cross-sectional dimension of the lesion at each lateral location.

(i.e., track, push, track, push). The system was in an F/1 focal configuration, and the transmit voltage was 140 Volts.

The curves in the top plot were generated using the same PRF for both the pushing and tracking pulses (3584 Hz), but different pulse lengths. As expected, the increase in steady state displacement is linearly related to the increase in pulse length (i.e., the increase in intensity). For example, the steady state displacement for the 3.4 microsecond pulse is double that of the 1.7 microsecond pulse. Also as expected, the time constants for displacement were similar for the different pulse lengths (~6 milliseconds, determined by fitting the curves to an exponential).

The bottom plot was generated using pushing beams with the same pulse length and transmit voltage, but with different PRFs (the PRF of the tracking beams was held constant at 3584 Hz). The frequency of the "rectified sine wave" apparent in each of the three curves corresponds to the PRF of the high intensity beams for each experiment. This temporal response is due to the recovery of the tissue between pushing beams. Note that the magnitude of the recovery increases with increasing mean tissue displacement. This recovery is not apparent in the top plot because the PRF of the tracking beams was the same as that for the pushing beams, thus the recovery response was undersampled. Again, as expected, the time constant for each of these curves was similar to those in the top plot (~6 milliseconds).

Figure 7 portrays the temporal response of Phantoms A, D, and the liver sample during force application and after removal of the force. The ramp-down time constants are 4.2, 1.5, and 7.9 milliseconds, respectively. This parameter is indicative of the damping present in the tissue. The ramp-up time for Phantom D is about the same (1.6 milliseconds), however it is slightly slower for Phantom A (5.1 milliseconds), and slightly faster for the liver sample (6.2 milliseconds).

### D. Multiple pushing locations with 2-D tracking regions

Figure 8 (top) provides a schematic showing the position of the different pushing locations (i.e. focal points) used in the multiple pushing location experiments, and their relationship to the lesion in Phantom C. The sub-plots show the displacement in the same spatial location as the pushing beam after 10 milliseconds of force application in each grid location. Each subplot represents the displacements obtained at all of the axial positions in one lateral location in the grid (as indicated by the letters a–f). The presence of the lesion is clear in these plots, where a "dip" in the axial profile occurs

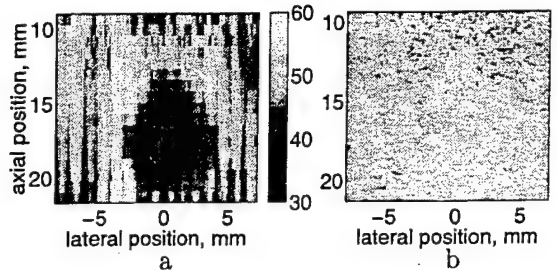


FIG. 9. (a) Displacement image created from multiple pushing locations in phantom C, corresponding to the raw data shown in Fig. 8. The pushing pulses were 1.7 microseconds long, with an F/1 focal configuration and a transmit voltage of 140 V. The PRF was 3584 Hz. The image was created by combining the displacements in each spatial location after 10 milliseconds of force application. The units of displacement on the colorbar are microns, and the transducer is at the top of the images. (b) Corresponding B-mode image.

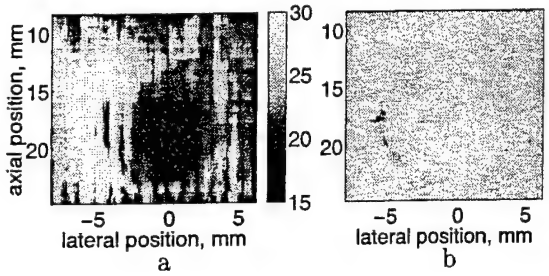


FIG. 10. (a) Displacement image created from multiple pushing locations in phantom B. This phantom had a tear between the lesion and the background material on the left side of the lesion. This resulted in some of the liquid phantom leaking into the tear, and hence a much more compliant region in the vicinity of the tear. The pushing pulses were 0.83 microseconds long, with an F/1 focal configuration and a transmit voltage of 140 V, and a PRF of 3584 Hz. The force applied in this experiment was half of that used to generate the image in Fig. 9. The image was created by combining the displacements in each spatial location after 10 milliseconds of force application. The units of displacement on the colorbar are microns, and the transducer is at the top of the images. (b) Corresponding B-mode image.

in each lateral location that intersected the lesion. The extent of the "dip" corresponds to the length of the interrogated cross-section of the lesion.

Figure 9(a) portrays the combination of all of the displacement data from the different pushing locations (from Fig. 8) into a single displacement image. In this image, the displacement at each pixel is determined by computing the average displacement from all of the pushing locations whose focal regions overlap with that pixel. The lesion is clearly apparent in the displacement image, while it is not as evident in the conventional B-mode image [Fig. 9(b)].

Figure 10(a) represents a combined displacement image of Phantom B that was generated in the same way as Fig. 9(a). Phantom B had a slight tear along the interface between the lesion and the background on the left side of the image. This region filled with the liquid slurry phantom material that surrounded the phantom. Therefore, it was much more compliant than the phantom itself. This is apparent in the displacement map shown in Fig. 10(a), as well as in the corresponding B-mode image [Fig. 10(b)].

## V. DISCUSSION

Several insights can be gained from the simplified point load analysis of radiation force (Fig. 1). This model is applicable to the lateral and elevation dimensions, where the size of the acoustic focal region is a fraction of a millimeter. It implies that RP can locally sample tissue stiffness with minimal confounding artifacts from neighboring tissue stiffness variations in these dimensions. In addition, because the strain and displacement fields are highly localized, displacements measured at the point of force application are highly correlated with tissue stiffness at that location.

The point load model is not directly applicable in the axial dimension, where the radiation force is distributed along a line (i.e., the focal region is approximately 1 cm axially). This does not, however, result in poor axial resolution. As shown in Fig. 8, the lesion boundary is preserved in all of the data where the axial extent of the focal region (i.e., the line of distributed force) crosses the lesion boundary.

Figures 9 and 10 clearly demonstrate the feasibility of acoustic remote palpation imaging. The homogeneous background medium is a fairly uniform gray color, and the stiffer lesion is clearly apparent as a darker region. The spatial extent of the lesions shown in these images is comparable to that in the corresponding B-mode images. The presence of the lesion is not apparent in the displacement maps beyond the lesion boundaries. This is clearly evident in Fig. 8, where the displacements on either side of the "dip" are very similar to those obtained in the same axial location in the absence of a lesion [e.g., subplots 8(d) and (f)]. This supports the hypotheses that remote palpation imaging can be performed in complex media without significant artifacts induced by neighboring structures, and that the displacements achieved in remote palpation imaging are directly correlated to tissue stiffness.

As predicted by finite element simulations,[26] the displacement profiles remain approximately the same shape for increases in intensity; and the displacement magnitude scales with intensity [Figs. 4(a) and (c)]. The slight decrease in the axial extent of the displacement profile, and the slight shift of the displacement peak towards the transducer in Fig. 4(c) is likely a result of nonlinear propagation of the higher pressure amplitude acoustic beam.[20,37] In both cases, the presence of the lesion results in a considerably different displacement profile.

In comparing Figs. 4(a) and (c), and Figs. 4(b) and (d), it is clear that the images generated at lower intensities exhibit more noise. This is due to the lower displacements in these images. The minimum detectable displacement for a correlation based tracking algorithm is dependent upon several factors: system signal-to-noise ratio (SNR), pulse-to-pulse correlation, signal bandwidth, as well as the center frequency and pulse length of the tracking beams. Utilizing values for the above parameters that are applicable to the experiments performed herein (i.e., 40 dB, 0.99, 70%, 7.2 MHz, 0.3 $\mu$s, respectively), the lower limit of displacement that can be tracked is computed to be 0.5$\mu$m.[38] The majority of the displacements in the low intensity cases [Figs. 4(a) and (b)] are close to this minimum detectable value, thus these displacement images have a lower signal-to-noise ratio (SNR) than those corresponding to the higher intensity beams [Figs. 4(c)

and (d)]. Clearly, larger displacements are preferable to achieve better SNRs.

Figure 5 represents the first *in vitro* remote palpation displacement maps generated in a tissue sample. Displacements of up to 15 microns were achieved in this tissue sample. The varying lateral focal point experiments were performed in order to investigate the limitations presented by a linear array with a fixed elevation focus. Each of the three maps was generated using an F/1 focal configuration and the same transmit voltage and pulse length. If the arrays were axi-symmetric (i.e., pistons), one would expect identically shaped displacement profiles, with decreases in peak displacement at deeper focal positions due to the attenuation of the overlaying tissue. However, because a linear array (asymmetric, 5 mm×20 mm) was used, the peak displacement actually occurs for the deepest focal position [Fig. 5(c)]. This focal position is closer to the elevational focal point than the other two focal positions, which results in increased intensities in this location. Remote palpation will ideally be implemented by holding the transducer in a stationary position, and using electronic focusing to apply radiation force to multiple pushing locations within an extended field of view (FOV). The implications of Fig. 5 are that some type of depth/focal position dependent scaling may be necessary to achieve a uniform displacement map in a homogeneous medium. This would be similar to time gain control (TGC), which is available on diagnostic scanners to account for tissue attenuation and focal gain. These results also suggest that a two-dimensional array capable of electronically focusing in both the lateral and elevation dimensions is preferable to a linear array.

Evaluation of the steady state displacements shown in the top of Fig. 6 indicates a linear relationship between steady state displacement and acoustic pulse length. Because increases in radiation force are proportional to increases in temporal average intensity (which are proportional to increases in pulse length), the steady state displacements shown in this plot portray a linear relationship between radiation force and temporal average intensity, which was predicted by finite element simulations.[26]

The bottom plot in Fig. 6 was generated using the same pushing pulses, with different PRFs. Therefore, the intensity was lower for the lower PRFs, which resulted in smaller steady state displacements. Because the PRF of the tracking pulses was fixed at 3584 Hz, which is above Nyquist for each of the pushing pulse PRFs, the bottom plot in Fig. 6 portrays the recovery of the phantom after each individual pushing pulse. This is apparent in the "rectified sine wave" that appears on each curve. The PRF of the pushing pulses is identical to the frequency of the "rectified sine wave" for each curve. It is interesting to note that for each curve, the magnitude of the recovery increases with increasing mean displacement (i.e., the amplitude of the rectified sine wave increases with time). In addition, the magnitude of the "rectified sine wave" is slightly larger for the lower PRFs. This is due to the recovery of the tissue between pushing pulses. The longer the time between pushing pulses, the more the tissue recovers resulting in a net "loss" in maximum displacement. This suggests that a more efficient method to implement remote palpation will be to use a single, very long pushing pulse, instead of the series of shorter duty cycle pushing pulses (1% to 3% duty cycles) used in these experiments.

This point is further demonstrated by evaluating the displacement after the same number of pulses have been fired at two different PRFs (Fig. 6, bottom). For example, at a PRF of 1280 Hz, after 6 milliseconds, 8 pushing pulses have been fired, and the displacement is 45 microns. Correspondingly, 8 pushing pulses have been fired at a PRF of 853 Hz after 8.5 milliseconds, and the displacement is 36 microns. If one computes the temporal average intensity used in both scenarios over 8.5 milliseconds, it is the same. However, by applying the energy initially, instead of evenly spacing it over the entire time, an increase of 20% is achieved in the maximum displacement.

Figure 7 allows the evaluation of the recovery time of two different phantoms and the liver sample. This quantity is indicative of the damping present in the tissue. The liver sample is clearly more damped than either of the phantoms, as it has a longer recovery time. Phantom D exhibits considerably less damping than the other two, in that its recovery curve appears almost linear.

As stated in the background section, remote palpation is similar to elastography, however it has many potential advantages. The fact that the radiation force field is localized and can be applied in selected remote locations is significant. Because the force is applied directly to the position of interest, considerably smaller forces are required than in the case of global compression. Thus one can achieve lesion detectability without exposing the tissue to potentially damaging larger strain fields. In addition, because displacement is directly correlated with local variations in stiffness, the method does not require complex reconstruction algorithms. Also, in contrast to elastography, the displacements generated during remote palpation are relatively small (microns). Thus the correlation based tracking routines are not subject to problems associated with relative scatterer motion in the presence of large strain.[39] Finally, remote palpation provides the ability to evaluate and image localized variations in the temporal response, or damping, of tissue.

Clinical implementation of remote palpation will be similar to conventional mixed modes, such as B-mode/color-mode. The physician will identify a smaller FOV within a B-mode image where remote palpation will be implemented. Then, upon entering the remote palpation mode, the physician will hold the transducer in a stationary position while the FOV is interrogated via electronic focusing and steering. Depending upon the size of the FOV, the spacing of the pushing locations, and the time spent at each location, frame rates as high as 2 to 5 frames per second may be achieved while interrogating a 1.5 cm square FOV. This frame rate will allow the superposition of remote palpation displacement images with the conventional B-mode image in semi-real-time, which will aid clinical evaluation.

The resolution achievable by remote palpation imaging systems will depend upon a variety of factors, including the size and spacing of the pushing beams, the resolution and spacing of the tracking beams, the target tissue mechanical

properties [Eqs. (4) and (5)], and the methods of image formation utilized. The impact of these factors on resolution is under investigation, however it is outside the scope of this paper.

Given the comparably high intensities and unique pulsing sequences of remote palpation imaging, the safety of the method is of concern. The phantoms used to create Figs. 9 and 10 had Young's moduli that were an order of magnitude lower than those of tissue, whereas phantom D was approximately four times more stiff than the liver sample. Detectable displacements were achieved in all of these media. The derated intensity used in the liver sample was approximately 80 W/cm$^2$. Accounting for the variability of tissue stiffnesses, this suggests that a reasonable upper limit on the *in situ* intensity required for *in vivo* remote palpation will be around 300 W/cm$^2$ at each pushing location (assuming an application time of several milliseconds). This is well in excess of the FDA limit (0.72 W/cm$^2$).[29] However, these high intensity beams need only be generated for time scales on the order of milliseconds. In this short time period, the heating that would be generated is less than 1 °C,[30] and is limited spatially to a region that is slightly smaller than the focal region of the acoustic beam. Therefore, assuming that adjacent pushing beams do not significantly overlap, the maximum expected temperature rise will be less than 1 °C. It is widely accepted that temperature increases of less than 1 °C do not pose a danger to the patient.[40] Thus, remote palpation imaging as discussed herein should not pose a danger to the patient.

## VI. CONCLUSION

The work presented herein demonstrates the feasibility of acoustic remote palpation. Displacement maps that are directly correlated with variations in tissue stiffness were generated and presented. It is possible to perform remote palpation using a single transducer on a diagnostic scanner to both generate the required high intensity beams, and track the resulting displacements. This will facilitate ease of implementation on transition to the clinical setting. The intensities that are required to induce detectable displacements *in vivo* (i.e., tens of microns) will be on the order of 200–300 W/cm$^2$, and the required dwell time less than 10 milliseconds. Due to the short duration of exposure, these beams should not cause appreciable tissue heating. Given these findings, acoustic Remote Palpation clearly exhibits clinical potential.

## ACKNOWLEDGMENTS

This work was supported by DOD BCRP Grant No. BC972755. We thank Siemens Medical Systems, Ultrasound Group for their system support. We thank Intel Corporation for their technical and in-kind support.

[1] A. Sarvazyan *et al.*, Acoust. Imaging **21**, 223 (1995).
[2] T. Krouskop *et al.*, Ultrason. Imaging **20**, 260 (1998).
[3] Y. Yamakoshi, J. Sato, and T. Sato, IEEE Trans. Ultrason. Ferroelectr. Freq. Control **17**, 45 (1990).
[4] R. Lerner, S. Huang, and K. Parker, Ultrasound Med. Biol. **16**, 231 (1990).
[5] K. Parker, S. Huang, R. Musulin, and R. Lerner, Ultrasound Med. Biol. **16**, 241 (1990).
[6] T. Krouskop, D. Dougherty, and S. Levinson, J. Rehabil. Res. Dev. **24**, 1 (1987).
[7] S. Levinson, J. Biomech. **20**, 251 (1987).
[8] J. Ophir *et al.*, Ultrason. Imaging **13**, 111 (1991).
[9] M. O'Donnell, A. Skovoroda, B. Shapo, and S. Emelianov, IEEE Trans. Ultrason. Ferroelectr. Freq. Control **41**, 314 (1994).
[10] J. Ophir *et al.*, Proc. Inst. Mech. Eng. **213**, 203 (1999).
[11] L. Gao, K. Parker, R. Lerner, and S. Levinson, Ultrasound Med. Biol. **22**, 959 (1996).
[12] B. Garra *et al.*, Radiology **202**, 79 (1997).
[13] P. J. Westervelt, J. Acoust. Soc. Am. **23**, 312 (1951).
[14] G. Torr, Am. J. Phys. **52**, 402 (1984).
[15] D. Christensen, *Ultrasonic Bioinstrumentation* (Wiley, New York, 1988).
[16] W. Nyborg, in *Physical Acoustics*, edited by W. Mason (Academic, New York, 1965), Vol. IIB, Chap. 11, pp. 265–331.
[17] D. Dalecki, Ph.D. thesis, University of Rochester, 1993.
[18] H. Starritt, F. Duck, and V. Humphrey, Phys. Med. Biol. **36**, 1465 (1991).
[19] A. Sarvazyan *et al.*, Ultrasound Med. Biol. **24**, 1419 (1998).
[20] O. Rudenko, A. Sarvazyan, and S. Emelianov, J. Acoust. Soc. Am. **99**, 2791 (1996).
[21] D. Dalecki, E. Carstensen, K. Parker, and D. Bacon, J. Acoust. Soc. Am. **89**, 2435 (1991).
[22] K. Nightingale, P. Kornguth, and G. Trahey, Ultrasound Med. Biol. **25**, 75 (1999).
[23] K. Nightingale and G. Trahey, IEEE Trans. Ultrason. Ferroelectr. Freq. Control **47**, 201 (2000).
[24] W. Walker, J. Acoust. Soc. Am. **105**, 2508 (1999).
[25] T. Sugimoto, S. Ueha, and K. Itoh, in *Proceedings of the 1990 Ultrasonics Symposium* (Publisher, City, 1990), pp. 1377–1380.
[26] K. Nightingale, R. Nightingale, M. Palmeri, and G. Trahey, Ultrason. Imaging **22**, 35 (2000).
[27] M. Fatemi and J. Greenleaf, Proc. Natl. Acad. Sci. U.S.A. **96**, 6603 (1999).
[28] S. Timoshenko and J. Goodier, *Theory of Elasticity* (McGraw-Hill, New York, 1987).
[29] Center for Devices and Radiological Health (CDRH), U.S. Dept of Health and Human Services, 1985, Rev. 1993 (1994).
[30] M. Palmeri, G. Trahey, R. Nightingale, and K. Nightingale, IEEE UFFC (in preparation).
[31] G. Trahey, J. Allison, and O. VonRamm, IEEE Trans. Biomed. Eng. **BME-34**, 965 (1987).
[32] NEMA Standards Publication/No. UD 2, *Acoustic Output Measurement Standard for Diagnostic Ultrasound Equipment* (National Electrical Manufacturers Association, Washington, DC, 1992).
[33] F. Duck, Ultrasound Med. Biol. **25**, 1009 (1999).
[34] T. J. Hall, M. Bilgen, M. F. Insana, and T. A. Krouskop, IEEE Trans. Ultrason. Ferroelectr. Freq. Control **44**, 1355 (1997).
[35] A. Skovoroda *et al.*, Biophysics (Engl. Transl.) **40**, 1359 (1995).
[36] E. J. Chen, J. Novakofski, W. K. Jenkins, and W. D. O'Brien, IEEE Trans. Ultrason. Ferroelectr. Freq. Control **43**, 191 (1996).
[37] A. Baker, Ultrasound Med. Biol. **23**, 1083 (1997).
[38] W. Walker and G. Trahey, IEEE Trans. Ultrason. Ferroelectr. Freq. Control **42**, 301 (1995).
[39] M. Bilgen and M. F. Insana, Phys. Med. Biol. **43**, 1 (1998).
[40] NCRP, *Report No. 113: Exposure Criteria for Medical Diagnostic Ultrasound: I. Criteria Based on Thermal Mechanisms* (National Council on Radiation Protection and Measurements, NCRP Publications, Bethesda, MD 20814, 1992).

## 10.2 In vivo clinical paper (submitted to UMB)

# Acoustic Radiation Force Impulse Imaging: In Vivo Demonstration of Clinical Feasibility [1]

Kathryn Nightingale [a,*] Mary Scott Soo [b] Roger Nightingale [a]
Gregg Trahey [a,b]

[a] *Department of Biomedical Engineering, Duke University, Box 90281, Durham, NC 27708-0281*

[b] *Department of Radiology, Duke University Medical Center, Box 3808, Durham, NC 27710*

**Abstract**

The clinical viability of a method of acoustic remote palpation, capable of imaging local variations in the mechanical properties of soft tissue using Acoustic Radiation Force Impulse (ARFI) imaging, is investigated *in vivo*. In this method, focused ultrasound is used to apply localized radiation force to small volumes of tissue (2 $mm^3$) for short durations (less than 1 msec) and the resulting tissue displacements are mapped using ultrasonic correlation based methods. The tissue displacements are inversely proportional to the stiffness of the tissue, and thus a stiffer region of tissue exhibits smaller displacements than a more compliant region. Due to the short duration of the force application, this method provides information about the mechanical impulse response of the tissue, which reflects variations in tissue viscoelastic characteristics. In this paper, experimental results are presented demonstrating that displacements on the order of ten microns can be generated and detected in soft tissues *in vivo* using a single transducer on a modified diagnostic ultrasound scanner. Differences in the magnitude and the transient response of tissue displacement are correlated with tissue structures in matched B-mode images. The results comprise the first *in vivo* ARFI images, and support the clinical feasibility of a radiation force based remote palpation imaging system.

*Key words:* Acoustic Radiation Force Impulse Imaging, Remote Palpation, Acoustic Radiation Force, Breast Ultrasound, Elastography

* Corresponding author: telephone:(919)660-5175, fax:(919)684-4488
*Email address:* kathy.nightingale@duke.edu (Kathryn Nightingale).

[1] Supported by grant DAMD17-98-1-8068 from the Department of Defense Breast Cancer Research Program, which is managed by the U.S. Army Medical Research and Materiel Command.

## 1 Introduction

The concept of assessing the material properties of a medium by monitoring its response to acoustic radiation force was first proposed by Sugimoto et. al. in 1990 (Sugimoto et al., 1990). In 1991, Dymling et. al. proposed the use of radiation force to characterize the viscous properties of a fluid (Dymling et al., 1991). Since then, several applications have been proposed. The viscous properties of milk (Dymling et al., 1991), *in vivo* cyst fluid (Nightingale et al., 1995, 1999), and blood (Hartley, 1997; Zauhar et al., 1998; Shi et al., 1999) have all been investigated, as have the visco-elastic properties of the vitreous humor (Walker et al., 2000), and the mechanical properties of soft tissue (Sarvazyan et al., 1998; Fatemi and Greenleaf, 1998; Nightingale et al., 2000).

Acoustic radiation force is a phenomenon associated with the propagation of acoustic waves through a dissipative medium. It is caused by a transfer of momentum from the wave to the medium, arising either from absorption or reflection of the wave (Torr, 1984). This momentum transfer results in the application of a body force in the direction of wave propagation. In an absorbing medium, and under plane wave assumptions, this force can be represented by the following equation (Torr, 1984; Nyborg, 1965; Dalecki, 1993; Starritt et al., 1991; Nightingale et al., 2000):

$$F = \frac{W_{absorbed}}{c} = \frac{2\alpha I}{c}, \tag{1}$$

where $F$ [dynes/(1000 cm$^3$)], or [kg/(s$^2$cm$^2$)] is acoustic radiation force, $W_{absorbed}$ [Watts/(100 cm$^3$)] is the power absorbed by the medium at a given spatial location, $c$ [m/s] is the speed of sound in the medium, $\alpha$ [m$^{-1}$] is the absorption coefficient of the medium, and $I$ [Watts/cm$^2$] is the temporal average intensity at a given point in space. For a focused acoustic beam, the radiation force is applied throughout the focal region of the acoustic beam.

Acoustic Radiation Force Impulse (ARFI) imaging is a new radiation force based imaging method that provides information about the local mechanical properties of tissue (Nightingale et al., 2001). ARFI imaging uses short duration acoustic radiation forces to generate localized displacements in tissue and these displacements are tracked using ultrasonic correlation based methods. The tissue response to these forces can be monitored both spatially and temporally. Displacement magnitude is inversely proportional to local tissue stiffness and is typically on the order of ten microns. Tissue velocity is related to tissue visco-elastic characteristics. The volume of tissue to which radiation force is applied is determined by the focal characteristics of the transmitting transducer, and is typically 1 to 8 mm$^3$. The period and temporal profile of the force application are determined by the transmitter pulse shape, with the duration of the force application limited to less than 1 millisecond. In this method, a single transducer on a diagnostic ultrasound system is used to both apply localized radiation forces within tissue for short time periods and to track the resulting tissue displacements. The use of a single transducer guarantees both alignment and ease of clinical implementation, as well as facilitating real-time implementation.

Two widely investigated methods that provide information about the stiffness of tissue are

elastography (Ophir et al., 1991; O'Donnell et al., 1994; Sarvazyan et al., 1995; Cespedes et al., 1995; Zhu et al., 1999) and sonoelasticity (Taylor et al., 2000; Muthupillai et al., 1995; Yamakoshi et al., 1990; Lerner et al., 1990; Parker et al., 1990; Krouskop et al., 1987; Levinson, 1987). In elastography, local variations in tissue strain are determined by measuring local displacements that occur during global tissue compression (Ophir et al., 1991; O'Donnell et al., 1994; Sarvazyan et al., 1995; Cespedes et al., 1995; Zhu et al., 1999). The Young's modulus of the tissue can then be reconstructed from these strain images. This method has shown some promise in differentiating benign from malignant lesions in the breast (Garra et al., 1997). In sonoelasticity, low frequency shear wave propagation is imaged using Doppler methods, from which the Young's modulus of tissue can be estimated (Taylor et al., 2000; Muthupillai et al., 1995; Yamakoshi et al., 1990; Lerner et al., 1990; Parker et al., 1990; Krouskop et al., 1987). ARFI imaging has some potential advantages over these methods, including the ability to locally sample tissue stiffness with minimal confounding artifacts from neighboring tissue stiffness variations, the decrease in maximum tissue strain required for lesion visualization, and the potential for real-time implementation without the need for external compression fixtures. In addition, ARFI imaging provides information about the dynamic temporal response of tissue (*i.e.* the mechanical impulse response of tissue), which is indicative of variations in tissue visco-elastic characteristics.

ARFI imaging has many potential clinical applications, including: detecting and characterizing a wide variety of soft tissue lesions, and identifying and characterizing atherosclerosis, plaque, and thromboses. In this paper, the following three hypotheses are investigated *in vivo*: first, that ARFI imaging can be implemented using a single transducer on a diagnostic scanner to generate and detect tissue displacements *in vivo*; second, that tissue structural information will be apparent in ARFI displacement maps; and third, that the transient response of tissue to radiation force will vary with tissue type.

## 2 Methods

Experiments were performed with a Siemens Elegra scanner (Siemens Medical Systems, Ultrasound Group, Issaquah, WA), that has been modified to allow user control of the acoustic beam sequences and intensities, as well as providing access to the raw radio-frequency (RF) echo data. A Siemens 75L40 linear array was used for these experiments. This array consists of 194 elements, each of which are 5 mm tall and approximately 0.2 mm wide, with a center frequency of 7.2 MHz. The number of active elements can be selected electronically to adjust the lateral transmit aperture width. There is a fixed-focus acoustic lens on each element that focuses in the elevation dimension. Lateral focusing is accomplished electronically by applying the appropriate delays to each active element.

The beam sequences used for these experiments consist of tracking beams and pushing beams. The tracking beams were standard diagnostic B-mode pulses (*i.e.* 7.2 MHz, 0.2$\mu$sec pulse length, F/1 focal configuration, apodized, $I_{spta.3}$ (derated spatial peak temporal average intensity) $< 0.1$ W/cm$^2$, MI (Mechanical Index: derated peak negative pressure divided by the square root of the center frequency) of 0.4, PRF (Pulse Repetition Frequency) of 5.6 kHz), and the system dynamically updates the focal point for these beams on receive. The

pushing beams were similar to those employed by this system for Doppler imaging, however they had much longer pulse lengths, and were applied at a 15% duty cycle for 0.7 milliseconds (*i.e.* 7.2 MHz, 28 $\mu$sec pulse length). The pushing beam transmit aperture utilized an F/1.5 focal configuration with no apodization, and achieved an $I_{spta.3}$ below 1000 W/cm$^2$, applied for 0.7 milliseconds, (i.e. 4 pulses at a PRF of 5.6 kHz), with an MI of 1.2. The pushing pulse echoes were not processed.

ARFI images were generated using nineteen pushing locations, each with the same focal depth (20 mm), separated laterally by 0.18 mm. Thus the lateral Region of Interest (ROI) of the resulting ARFI images was 3.6 mm. At each pushing location alternating tracking and pushing lines were fired along the same line of flight (*i.e.* A-line interrogation). The PRF for these experiments was 11264 Hz, thus the PRF for both the tracking and pushing beams was 5632 Hz. The first beam fired was a tracking beam which served as a reference for the initial tissue position. Then a series of four pushing beams interspersed with tracking beams were fired. These interspersed beams were immediately followed by 21 tracking beams which allowed observation of the temporal response of the tissue after removal of radiation force. The time spent at each pushing location was 4.6 msec; acquisition of data from all 19 pushing locations took 90 msec. The raw RF echo data was stored and processed off-line.

### *2.1 Method Safety*

The MI of the pushing beams used for ARFI imaging is less than the United States Food and Drug Administration (US FDA) limit of 1.9, and is consistent with those used in Color Doppler imaging. Therefore, the potential for generating non-thermal bioeffects (i.e. cavitation) with the ARFI pushing beams is no greater than that for conventional Color Doppler pulse sequences with a similar MI.

A worst-case estimate of the potential temperature increase resulting from the pushing beams used in ARFI imaging can be estimated by solving the bio-heat transfer equation (Pennes, 1948) neglecting convection and conduction (Nyborg, 1988; NCRP, 1983). Under these assumptions, the equation becomes a first order linear differential equation, whose solution provides a linear relationship between temperature increase and application time:

$$\Delta T = \frac{q_v}{\gamma_v} t = \frac{2\alpha I}{\gamma_v} t, \tag{2}$$

where $\Delta T$ is the increase in temperature, $q_v$ is the rate of heat production per unit volume, $\gamma_v$ is the volume specific heat for tissue, $\alpha$ is the absorption coefficient of tissue, $I$ is the temporal average intensity of the acoustic beam in a given spatial location, and $t$ is the application time. For the pushing beams used in ARFI imaging, the peak anticipated temperature increase in each pushing location is 0.14 °C ($\alpha$=0.415 Np/cm (i.e. 0.5 dB/cm/MHz at 7.2 MHz), $I$=1000 W/cm$^2$ (*in situ*), $\gamma_v$=4.2 Joules/(cm$^3$°C), t = 0.7 msec). The spatial separation of the pushing locations results in minimal accumulation of heat between locations. Thermal increases less than 1.0°C are considered acceptable during diagnostic ultrasound scanning (Center for Devices and Radiological Health (CDRH), 1994; NCRP, 1992), and thus the ARFI beam sequences used in these experiments do not pose an increased risk to the patient over that

of conventional ultrasound imaging.

### *2.2 Data Processing*

The summed RF echo data is 16 bit data, acquired from the Elegra scanner at a sampling rate of 36 MHz. The data is up-sampled to 4.3 GHz, thus given an assumed acoustic velocity of 1540 m/s the minimum measured displacement is 0.18 microns. Off-line data processing was accomplished by performing 1-D cross-correlation in the axial dimension between the up-sampled sequentially acquired tracking lines (Trahey et al., 1987; O'Donnell et al., 1994). Each tracking line was divided into a series of search regions (0.33 mm in length), and the location of the peak in the cross correlation function between a kernel in the first tracking line (0.27 mm in length) and the corresponding search region in the next tracking line was used to estimate the axial tissue displacement in that region. A 75% overlap of the kernel regions was used. The resulting datasets allow the monitoring of tissue displacement through time both during and after force application.

### *2.3 ARFI Image Formation*

The complete ARFI dataset includes displacement through time throughout a two-dimensional ROI. Because the measured tissue velocities are comparable to those induced by cardiac and respiratory motion (*i.e.* 3.7 microns of motion in 4.6 msec, assuming a velocity of 0.8 mm/sec (El-Fallah et al., 1997)), displacements due to radiation force can be obscured by cardiac and respiratory motion. A simple motion filter was devised to remove these artifacts. At each spatial location, a linear fit to the displacement data is computed from time step 0 (with 0 displacement) to the last time-step (4.6 msec), at which time the tissue is expected to have returned to its original position. The slopes of these lines are averaged using a 0.1 mm axial sliding window, and this linear component is subtracted from the temporal displacement data at each spatial location, with the remaining displacements being attributed to radiation force. ARFI displacement images are generated by combining the data from each spatial location at each time step. These images are superimposed over matched B-mode images.

In addition to images of tissue displacement, images of the time it takes for the tissue to reach its peak displacement, and tissue recovery velocity (*i.e.* the slope of the displacement/time curve as the tissue recovers to its initial position) are presented.

### *2.4 Clinical Implementation*

The transducer was hand-held for these experiments. Once an ROI had been identified using conventional B-mode, the custom pulse sequence was fired (as described above), and echo data was stored for off-line processing. After firing the custom pulse sequence, the system stopped transmitting, the transmit beam software was updated, and the corresponding B-mode image frame was acquired within 1 second. Each acquisition took approximately 2 minutes, including transducer positioning, data acquisition, and data storage. Experiments were performed in the abdomen, bicep, and thyroid of the authors, as well as in the breast of one patient under the guidance of the IRB approved clinical protocol.

## 3 Results

In a homogeneous tissue mimicking phantom, the ARFI pulse sequence produced a displacement profile that was consistent with the size of the focal region of the pushing beams immediately after force application (Figure 1a). The white region, corresponding to a displacement of 14 microns away from the transducer, extends axially along the length of the focal region of the pushing beam. The phantom exhibited a complex transient response to the ARFI beam sequence (Figure 1b). Note that the peak in displacement first occurs at the focus (20 mm) at 0.8 msec. This peak then propagates axially away from the focus (both toward and away from the transducer), with peaks in displacement occurring later in time increasingly farther from the focus (*i.e.* the peaks at 15 and 25 mm occur later than that at 20 mm, but earlier than that at 10 mm). In addition, the apparent width of the peak increases with distance from the transducer. This increase in width is associated with decreasing tissue velocities (*i.e.* slope of the displacement/time curve). Throughout this paper, these tissue velocities will be referred to as the excitation velocity (slope of the displacement/time curve during the application of radiation force (0 through 0.7 msec)), and the recovery velocity (slope of the displacement/time curve as the tissue recovers from its peak displacement to its original position).

In the human bicep, the ARFI pulse sequence produced displacements with variations in magnitude that were correlated with layered structures in the matched B-mode image (Figure 2a). The layered structures in the B-mode image at 9, 14, 20, and 23 mm in depth are clearly portrayed in the ARFI image. The transient response of the bicep is more complex than that of the phantom (Fig. 2b). The tissue at depths 17 and 20 mm exhibits higher excitation velocities than at depths 23 and 8 mm, with the tissue at 13 mm exhibiting the slowest excitation velocity. In addition, the tissue at 8 mm exhibits a faster recovery velocity than that at any other depth.

In the thyroid, the displacement magnitude was nearly uniform over the majority of the gland immediately after cessation of radiation force (Figure 3a). Note that there is no speckle in the ARFI image. The speckle signal to noise ratio (SNR, $\frac{\mu}{\sigma}$) of the region of tissue within the thyroid is 6.1 in the ARFI image, as compared to 1.7 in the B-mode image. The recovery velocities within the thyroid tissue are slower than those of the tissue above it (Fig. 3b). The peak in displacement occurs later in time at depths 8-15 mm than it does at depths 20 and 21 mm. In contrast to the phantom and bicep images (Figs. 1b, 2b), the excitation velocities are nearly the same at all tissue depths.

In the abdomen, the ARFI displacement image immediately after force cessation shows good correlation with layered structures apparent in the matched B-mode image (Figure 4a). For example, in the ARFI image, the band of tissue at 23 mm is clearly differentiated as a stiffer region of tissue (*i.e.* a region of decreased displacement). In some cases, the displacements are lower for brighter B-mode structures (i.e. depth of 23 mm), and in some cases the displacements are larger (i.e. depth of 14 mm).

Both the excitation and recovery tissue velocities vary with depth in the abdomen (Fig. 4b). In general, the excitation velocities decrease with increasing distance from the focus (20

mm). The exception is that the excitation velocity of the band of tissue at 23 mm is much slower than that of the tissue beneath it. This band of tissue also exhibits a much slower recovery velocity than other tissues.

In the breast, there appears to be good correlation between the ARFI image and the matched B-mode image from 5 to 30 mm in depth (Figure 5a). The lesion is portrayed in the ARFI image as a stiffer region (i.e. smaller displacement) surrounding a noisier slightly softer region (i.e. larger mean displacement). This lesion was determined to be an infected lymph node by core biopsy.

The excitation velocities in the breast at depths of 7, 10 and 15mm are higher than those at depths of 3, 20 and 25mm (Fig. 5b). In addition, the recovery velocities at 20, 25, and to a lesser extent 15 mm are slower than those at the other depths.

The transient response to ARFI excitation in the breast varies with tissue structure. For example, in Fig. 6, the region of tissue on the left side of the image spanning from 13 to 18 mm (corresponding to a structure in the B-mode image) moves farther, and exhibits a later peak displacement than any other region of tissue. Note that this region of tissue is slightly darker than the surrounding tissue in the matched B-mode image. In addition, there is a region of tissue located at 10 mm on the right side of the ARFI image that also takes longer to reach its peak displacement, but recovers more quickly than its surrounding tissue. In contrast to the feature on the left side, this region of tissue corresponds to a slightly brighter region in the matched B-mode image.

In addition to images of displacement at 0.8 msec, images of the time it takes for tissue to reach its peak displacement and images of recovery velocity allowed the differentiation of some tissue structures (Fig. 7). Each of these images show good correlation with tissue structures in the matched B-mode image.

The axial extent of the region of tissue over which appreciable radiation force is applied appears to be larger than the focal region of the pushing beams in some tissues (Fig. 8). The phantom and bicep portray strong peaks in displacement near the focus, the axial extent of which is consistent with the size of the axial extent of the focal region of the pushing beams. However, the other tissues do not exhibit strong peaks near the focus. The band of tissue at 23 mm in the abdomen is apparent as a dip in the displacement curve, as are the boundaries of the breast lesion at 20 and 24 mm. The peak in the breast data occurs near 10 mm, well in front of the focus (20 mm).

## 4 Discussion

The results presented herein represent the first *in vivo* Acoustic Radiation Force Impulse images. Peak displacement magnitudes range from 5 to 13 microns *in vivo*. In general, variations in displacement magnitude in the ARFI images are highly correlated with structures in the matched B-mode images. For example, the lesion in the B-mode image of the breast exhibits a stiff outer boundary, with a softer interior in the matched ARFI image (Fig. 5). Core biopsy of this lesion demonstrated an infected lymph node, with a central more liquid

abscessed component. This pathology is consistent with a softer inner core surrounded by a stiffer encapsulating region of tissue. While these findings are circumstantial, they do suggest potential correlation between the clinical pathology and the ARFI image. In some cases brighter structures in the B-mode image appear softer than the surrounding tissue (*i.e.* they move farther: Fig. 4 at 14mm, and Fig. 5 at 10mm), and in some cases they appear stiffer (*i.e.* Fig. 4 at 23mm). This indicates that, as expected, tissue brightness in a B-mode image is not directly related to tissue stiffness. These findings support our first two hypotheses: that ARFI images can be generated *in vivo*, and that tissue structures will be apparent in ARFI images.

There is no speckle in the ARFI images. Thus, the traditionally defined speckle SNR of a conventional ultrasound imaging system (*i.e.* $\frac{\mu}{\sigma}$, which has a maximum value of 1.91 (Goodman, 1996)) is in general lower than that of an ARFI imaging system. For example, in Fig. 3, the speckle SNR in the thyroid is more than three times larger in the ARFI image than in the matched B-mode image (6.1 vs. 1.7). Comparison of the contrast of the ARFI and B-mode images yields variable results. The contrast is computed to be the ratio of the mean brightness (B-mode image) or displacement (ARFI image) in two matched ROIs within the images, with the highest value in the numerator. For example, in Fig. 3, the contrast between the thyroid and the tissue above it is 1.6 in the B-mode image, and 1.2 in the ARFI image. In the abdomen, the contrast between the band of tissue at 23 mm and the tissue above it is 1.1 in the B-mode image, and 2.0 in the ARFI image. These differences are expected, because the images represent different tissue properties.

The radiation force and resulting tissue displacements are predominantly in the direction of wave propagation. With the imaging geometry used in ARFI imaging, only these axial displacements are tracked. While useful information might be derived from the lateral components of displacement, they are expected to be very small (i.e. less than 1 micron), and direct ultrasonic tracking of such small displacements is extremely challenging. The theoretical lower limit on the displacement that can be tracked using correlation based algorithms can be estimated using the Cramer-Rao Lower Bound (Walker and Trahey, 1995). Assuming a good signal-to-noise ratio (60 dB), and a high correlation between the reference and tracking lines (0.998), the estimated lower limit on the axial displacement that can be tracked in the ARFI data is 0.5 microns. For the majority of the data in the ARFI datasets, these assumptions are valid. However, within the breast lesion in Fig. 5, the correlation values are lower (0.989), and thus the jitter error is more than doubled (1.2 microns). This results in a noisier image in this region.

Different tissues exhibit different transient responses to the ARFI pushing beams. Fig. 7 allows the differentiation of tissue structures based on displacement magnitude at 0.8 msec, the time it took for the tissue to reach its maximum displacement, and the recovery velocity of tissue. This supports the third hypothesis of this paper, that differences in the transient response of tissue may be used to characterize tissue. In media where simple tissue models are applicable (such as the Voigt model (Walker et al., 2000)), one could derive mechanical properties from such parametric images. However, evaluation of the transient response of soft tissue to ARFI excitation is complex. The factors affecting the measured local transient

response of tissue to ARFI excitation include the following: the local tissue visco-elastic properties and tissue density; the local magnitude of radiation force, the properties of the surrounding tissue (*i.e.* the boundary conditions); and the generation and propagation of shear waves. The combination of these effects make it difficult to form images of specific material properties from the ARFI displacement data. However, this situation is similar to that of conventional ultrasonic B-mode imaging and MRI, in that the images provide anatomic detail without imaging a specific material property. There are a myriad of methods from which the measured displacement data can be used to generate potentially useful images. Examples of which are shown in Figure 7. In addition, varying the characteristics of the pushing and tracking beams (*i.e.* look direction, focal characteristics, timing, intensity, transmit frequency) should allow improved visualization of more specific material properties.

An interesting phenomenon that is evident in the *in vivo* ARFI images is the apparent increase in length of the axial dimension of the volume of tissue over which radiation force is applied over that observed in the phantom (Fig. 8). In the phantom, the axial displacement profile exhibits a strong peak near the focus, which is consistent with the size of the focal region of the pushing beams. In the bicep, while structural information is apparent from depths of 5 to 30 mm, there also appears to be a strong peak in the axial displacement profile within the focal region of the pushing beams. This peak could be attributed to softer tissue in this region, or, more likely, it could be attributed to an increase in the local radiation force due to the focal gain of the acoustic beam. However, the thyroid, abdomen, and breast do not exhibit strong peaks near the focal region. The clear portrayal of structural information in these tissues from 5 to 30 mm seems to suggest that radiation force of appreciable magnitude was applied over this entire range. In other words, there is no apparent focal gain in these images. While the exact cause of this focal region 'stretching' is unclear, it is likely related to differences in absorption ($\alpha$) and possibly nonlinearity of the different tissues. The cause of this phenomenon is under investigation.

The resolution of an ARFI imaging system will depend on several factors, including transducer parameters, number of pushing locations, spatial relationship of pushing locations and tracking beams, and the pulse length and kernel size used for the tracking algorithm. As with elastography, in addition to these system parameters, the resolution will also be impacted by the tissue itself. The images shown herein suggest that the resolution of an ARFI imaging system will be at least comparable to that achieved in conventional B-mode imaging. For example, the upper boundary of the lesion in Fig. 5 is slightly angled and the ARFI image portrays comparable axial and lateral resolution to the matched B-mode image; in addition, the upper thyroid boundary in Fig. 3 is clearly apparent in both the ARFI and matched B-mode images.

The acoustic energy required to generate detectable displacements *in vivo* is large, and has the potential to generate increases in tissue temperature. However, the tissue displaces quickly, thus the application of high acoustic intensities (less than 1000 W/cm$^2$ *in situ*) is limited to a short time span (0.7 msec in each pushing location). It has been suggested that it is not possible to generate detectable displacements using radiation force in soft tissue while maintaining a temperature increase below 1°C (Walker et al., 2000; Fatemi and Greenleaf,

2000). These statements are based upon a steady state assumption, which is not applicable to ARFI imaging. As shown by Eqn. 2, the intensities and application times of the pushing pulses used for ARFI imaging are safe, and will not result in an increase in risk to the patient over that associated with conventional diagnostic ultrasound imaging.

## 5 Conclusion

The feasibility of ARFI imaging has been established by demonstration of *in vivo* studies. Using a single transducer on a modified diagnostic scanner, tissue displacements on the order of ten microns were generated using acoustic radiation force and detected using ultrasonic correlation based methods *in vivo*. Differences in displacement maps are correlated with tissue structure as observed in matched B-mode images. The transient response of tissue varied with tissue type, suggesting a possible application of ARFI imaging in differentiating tissues based on differences in their visco-elastic behavior. Although these findings are preliminary, they present several opportunities for ARFI imaging, and indicate that this method holds considerable clinical promise.

## References


Center for Devices and Radiological Health (CDRH). 510(k) guide for measuring and reporting acoustic output of diagnostic ultrasound medical devices. U S Dept of Health and Human Services 1985, Rev. 1993, 1994.

Cespedes, I.; Insana, M.; Ophir, J. Theoretical bounds on strain estimation in elastography. IEEE Transactions on Ultrasonics, Ferroelectrics and Frequency Control 42(5):969–72, 1995.

Dalecki, D. Mechanisms of Interaction of Ultrasound and Lithotripter Fields with Cardiac and Neural Tissues. Ph.D. thesis, University of Rochester, 1993.

Dymling, S.; Persson, H.; Hertz, T.; Lindstrom, K. A new ultrasonic method for fluid property measurements. Ultrasound Med. Biol. 17:497–500, 1991.

El-Fallah, A.; Plantec, M.; Ferrara, K. Ultrasonic measurement of breast tissue motion and the implications for velocity estimation. Ultrasound in Medicine and Biology 23(7):1047–57, 1997.

Fatemi, M.; Greenleaf, J. Ultrasound-stimulated vibro-acoustic spectrography. Science 280:82–85, 1998.

Fatemi, M.; Greenleaf, J. Probing the dynamics of tissue at low frequencies with the radiation force of ultrasound. Phys. Med. Bio. 45(6):1449–1464, 2000.

Garra, B.; Cespedes, E.; Ophir, J.; Spratt, S.; Zuurbier, R.; Magnant, C.; Pennanen, M. Elastography of breast lesions: Initial clinical results. Radiology 202:79–86, 1997.

Goodman, J. Introduction to Fourier Optics. New York: McGraw-Hill Companies, Inc., 1996.

Hartley, C. Characteristics of acoustic streaming created and measured by doppler ultrasound. IEEE Trans. Ultrason., Ferroelec., Freq. Contr. 44(6):1278–1285, 1997.

Krouskop, T.; Dougherty, D.; Levinson, S. A pulsed doppler ultrasonic system for making noninvasive measurements of the mechanical properties of soft tissue. J. Rehabil. Res. Dev. 24:1–8, 1987.

Lerner, R.; Huang, S.; Parker, K. Sonoelasticity images derived from ultrasound signals in mechanically vibrated tissues. Ultrasound Med. Biol. 16:231–239, 1990.

Levinson, S. Ultrasound propagation in anisotropic soft tissues, the application of linear elastic theory. J. Biomech. 20:251–260, 1987.

Muthupillai, R.; Lomas, D.; Rossman, P.; Greenleaf, J.; Munduca, A.; Ehman, R. Magnetic resonance elastography by direct visualization of propagating acoustic strain waves. Science 269:1854–1857, 1995.

NCRP. Report No. 74: Biological Effects of Ultrasound: Mechanisms and Clinical Implications. NCRP Publications, Bethesda, MD 20814: National Council on Radiation Protection and Measurements, 1983.

NCRP. Report No. 113: Exposure Criteria for Medical Diagnostic Ultrasound: I. Criteria Based on Thermal Mechanisms. NCRP Publications, Bethesda, MD 20814: National Council on Radiation Protection and Measurements, 1992.

Nightingale, K.; Kornguth, P.; Trahey, G. The use of acoustic streaming in breast lesion diagnosis: a clinical study. Ultrasound Med. Biol. 25(1):75–87, 1999.

Nightingale, K.; Kornguth, P.; Walker, W.; McDermott, B.; Trahey, G. A novel ultrasonic technique for differentiating cysts from solid lesions: Preliminary results in the breast. Ultrasound Med. Biol. 21(6):745–751, 1995.

Nightingale, K.; Nightingale, R.; Palmeri, M.; Trahey, G. A finite element model of remote palpation of breast lesions using radiation force: Factors affecting tissue displacement. Ultrasonic Imaging 22(1):35–54, 2000.

Nightingale, K.; Palmeri, M.; Nightingale, R.; Trahey, G. On the feasibility of remote palpation using acoustic radiation force. J. Acoust. Soc. Am. 110(1):625–634, 2001.

Nyborg, W. Acoustic streaming. In: Mason, W., ed., Physical Acoustics, New York: Academic Press Inc, vol. IIB, chap. 11, 265–331. 1965.

Nyborg, W. Solutions of the bio-heat transfer equation. Phys. Med. Biol. 33:785–792, 1988.

O'Donnell, M.; Skovoroda, A.; Shapo, B.; Emelianov, S. Internal displacement and strain imaging using ultrasonic speckle tracking. IEEE Trans. Ultrason., Ferroelec., Freq. Contr. 41:314–325, 1994.

Ophir, J.; Cespedes, I.; Ponnekanti, H.; Yazdi, Y.; Li, X. Elastography: A quantitative method for imaging the elasticity of biological tissues. Ultrasonic Imaging 13:111–134, 1991.

Parker, K.; Huang, S.; Musulin, R.; Lerner, R. Tissue response to mechanical vibrations for sonoelasticity imaging. Ultrasound Med. Biol. 16:241–246, 1990.

Pennes, H. Analysis of tissue and arterial blood temperatures in the resting human forearm. J. Appl. Physiol. 1:93–122, 1948.

Sarvazyan, A.; Rudenko, O.; Swanson, S.; Fowlkes, J.; Emelianov, S. Shear wave elasticity imaging: A new ultrasonic technology of medical diagnostics. Ultrasound Med. Biol. 24(9):1419–1435, 1998.

Sarvazyan, A.; Skovoroda, A.; Emelianov, S.; Fowlkes, J.; Pipe, J.; Adler, R.; Buxton, R.; Carson, P. Biophysical bases of elasticity imaging. Acoustical Imaging 21:223–240, 1995.

Shi, X.; Martin, R.; Vaezy, S.; Crum, L. Color doppler imaging of acoustic streaming in blood and clot. IEEE Ultrason. Symp. 1315–1318, 1999.

Starritt, H.; Duck, F.; Humphrey, V. Forces acting in the direction of propagation in pulsed ultrasound fields. Phys. Med. Biol. 36:1465–1474, 1991.

Sugimoto, T.; Ueha, S.; Itoh, K. Tissue hardness measurement using the radiation force of focused ultrasound. In: Proceedings of the 1990 Ultrasonics Symposium. 1990, 1377–1380.

Taylor, L.; Porter, B.; Rubens, D.; Parker, K. Three-dimensional sonoelastography: Principles and practices. Phys. in Med. Biol. 45:1477–1494, 2000.

Torr, G. The acoustic radiation force. Am. J. Phys. 52:402–408, 1984.

Trahey, G.; Allison, J.; VonRamm, O. Angle independent ultrasonic detection of blood flow. IEEE Trans. Biomed. Egr. BME-34(12):965–967, 1987.

Walker, W.; Fernandez, F.; Negron, L. A method of imaging viscoelastic parameters with acoustic radiation force. Phys. Med. Bio. 45(6):1437–1447, 2000.

Walker, W.; Trahey, G. A fundamental limit on delay estimation using partially correlated speckle signals. IEEE Trans. Ultrason., Ferroelec., Freq. Contr. 42(2):301–308, 1995.

Yamakoshi, Y.; Sato, J.; Sato, T. Ultrasonic imaging of internal vibration of soft tissue under forced vibration. IEEE Trans. Ultrason., Ferroelec., Freq. Contr. 17(2):45–53, 1990.

Zauhar, G.; Starritt, H.; Duck, F. Studies of acoustic streaming in biological fluids with an ultrasound doppler technique. British Journal of Radiology 71:297–302, 1998.

Zhu, Y.; Chaturvedi, P.; Insana, M. Strain imaging with a deformable mesh. Ultrasonic Imaging 21(2):127–146, 1999.

Figure 1: a) ARFI image of tissue displacement at time 0.8 msec (right, overlaid on top of the B-mode image), and matched B-mode image (left) in a homogeneous tissue mimicking phantom. The transducer is located at the top of the images, and the colorbar scale is microns. The white region in the ARFI image, corresponding to a displacement of 14 microns, extends axially along the length of the focal region of the pushing beam (approximately 3 mm). b) displacement through time at different depths (as indicated in mm in the legend) in the center of the ARFI image (0 mm laterally). Note that in this homogeneous phantom, propagation of the peak displacement toward and away from the focal region is apparent both as a decrease in the excitation and recovery velocities (*i.e.* the slopes of the curve during and after force application, respectively) as well as a delay in the location of the peak displacement with increasing distance from the focus (20 mm).

Figure 2: a) ARFI displacement image at time 0.8 msec (right), and matched B-mode image (left) in the bicep of the third author. The transducer is located at the top of the images, and the colorbar scale is microns. The layered structures exhibit good correlation between the B-mode and ARFI images (*i.e.* at depths of 9, 14, 20, and 23 mm). The boundary of the fibrous tissue layer between the muscles at 14mm is delineated by a dark region in the ARFI image, and the upper boundary of the fibrous band at 20 mm is delineated by a bright region in the ARFI image. b) displacement through time at different depths (as indicated in mm in the legend) in the center of the ARFI image (0 mm laterally). The excitation velocities are greatest near the focus (17 and 20 mm), and the recovery velocity is slowest at a depth of 13 mm.

Figure 3: a) ARFI image of displacement at 0.8 msec (right), and matched B-mode image (left) in the thyroid of the last author. The transducer is located at the top of the images, and the colorbar scale is microns. The thyroid (11 to 21 mm in depth) is clearly apparent in the ARFI image as a region of nearly uniform displacement of 3 microns. b) displacement through time at different depths (as indicated in mm in the legend) in the center of the ARFI image (0 mm laterally). Note that in contrast to the phantom (Fig. 1b), the tissue at all depths exhibits similar excitation velocities. In addition, the recovery velocity at a depth of 8 mm (above the thyroid) is much faster than those within the thyroid.

Figure 4: a) ARFI image of tissue displacement at 0.8 msec (right), and matched B-mode image (left) in the abdomen of the last author. The transducer is located at the top of the images, and the colorbar scale is microns. A 10 mm non-attenuating standoff pad was used for this acquisition. There is good correlation between layered structures in the ARFI image and the underlying B-mode image. The band of tissue at 23 mm appears to be stiffer than the surrounding tissue (*i.e.* it does not move as far as other tissues). The layer of skin at the top of the image (10 - 13 mm) appears to move uniformly, with a smaller magnitude than the underlying tissue. b) displacement through time at different depths (as indicated in mm in the legend) in the center of the ARFI image (0 mm laterally). Note that the band of tissue at 23 mm exhibits slower excitation and recovery velocities than the surrounding tissues.

Figure 5: a) ARFI image of tissue displacement at 0.8 msec (right), and matched B-mode image (left) in an *in vivo* female breast. The transducer is located at the top of the images, and the colorbar scale is microns. There is a lesion located on the right side of the images between 20 and 25 mm that is evident as a darker region of tissue in the B-mode image (white arrow). This lesion was palpable, and upon aspiration was determined to be an infected lymph node. In the ARFI image, the lesion boundary appears stiffer than its interior and the tissue above it (*i.e.* it exhibits smaller displacements). In addition, the oval structure in the B-mode image immediately above and to the left of the lesion (black arrow) appears to be outlined as a softer region of tissue than its surroundings in the ARFI image. b) displacement through time at different depths (as indicated in mm in the legend) in the center of the ARFI image (0 mm laterally). The tissue at depths of 7, 10 and 15 mm exhibits faster excitation and recovery velocities than that at 20, 25, and 3 mm.

Figure 6: ARFI images at times 0.4 msec (a), 1.2 msec (b), 2.1 msec (c), and 3.0 msec (d) in the *in vivo* female breast (generated from the same dataset as the data shown in Fig 5). The transducer is located at the top of the images, and the colorbar scale is microns. Note that the oval structure immediately above and to the left of the lesion in the B-mode image (Fig. 5a, left, black arrow) appears to be softer than the tissue to its right. In addition, it takes longer to reach its peak displacement than the surrounding tissue.

Figure 7 B-mode image, ARFI image of tissue displacement at 0.8 msec, ARFI image of the time it took for the tissue to reach its peak displacement, and ARFI image of the tissue recovery velocity from the *in vivo* breast data. Note the reversal in contrast between the time to peak displacement and recovery velocity images. For example, the tissue above the oval structure on the left side of the B-mode image is darker in the time to peak image, and brighter in the recovery velocity image, whereas the oval structure exhibits the opposite behavior.

Figure 8 Normalized mean displacement vs. depth (averaged laterally across all 19 pushing locations) from Figs. 1- 5. Each curve was normalized by its peak value, and then scaled to a different value in order to allow observation of the curve shape (phantom by 0.3, bicep by 0.5, abdomen by 0.7, thyroid by 1.1 and breast by 1.3). The curve for the abdomen does not include the standoff pad, thus it begins at the surface of the skin (10 mm axially). Note that the phantom and the bicep exhibit strong peaks in displacement near the focus, however a strong focal peak is not apparent in the thyroid, breast, or abdomen.

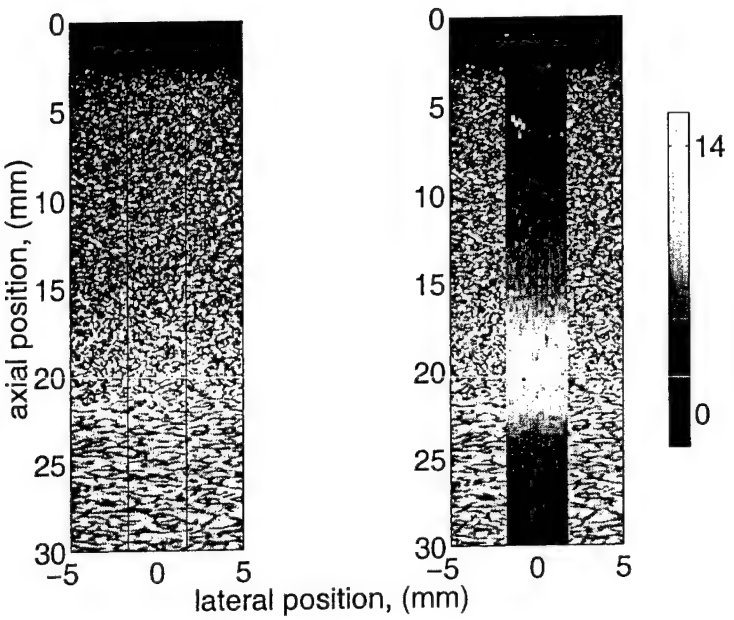


a

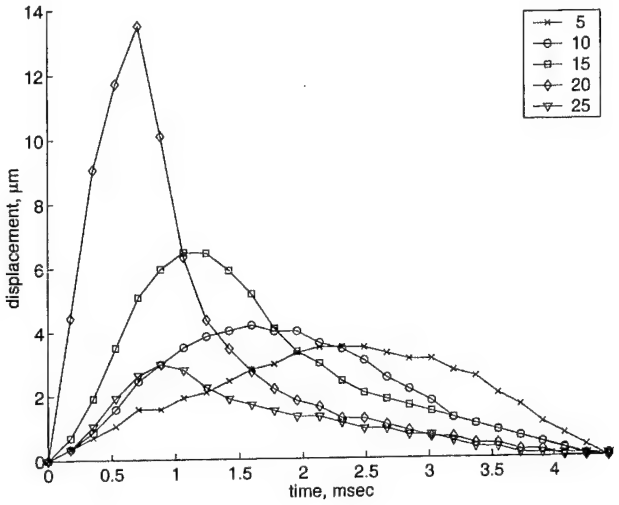


b

Fig. 1.

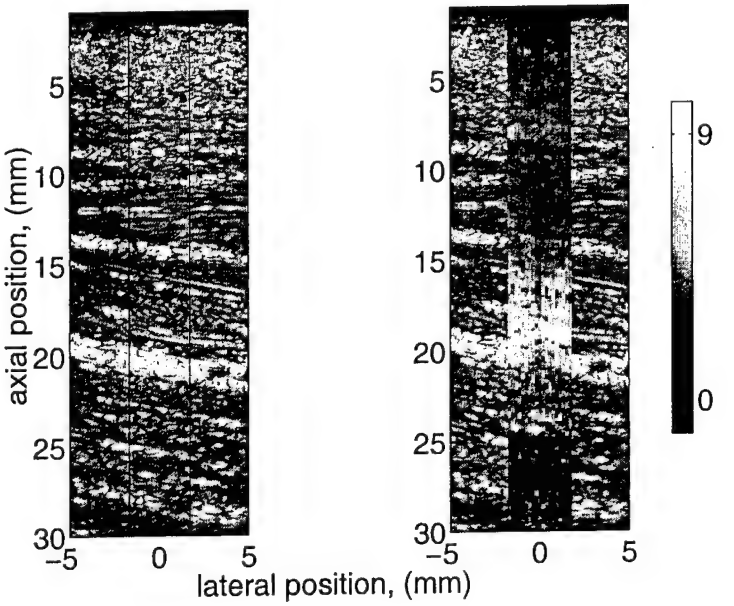


a

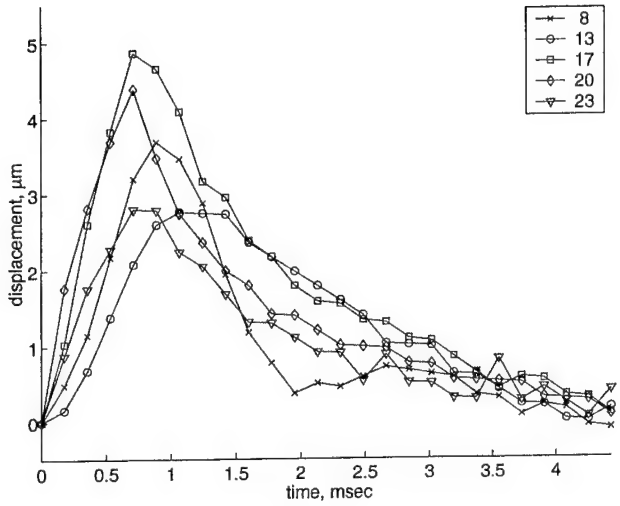


b

Fig. 2.

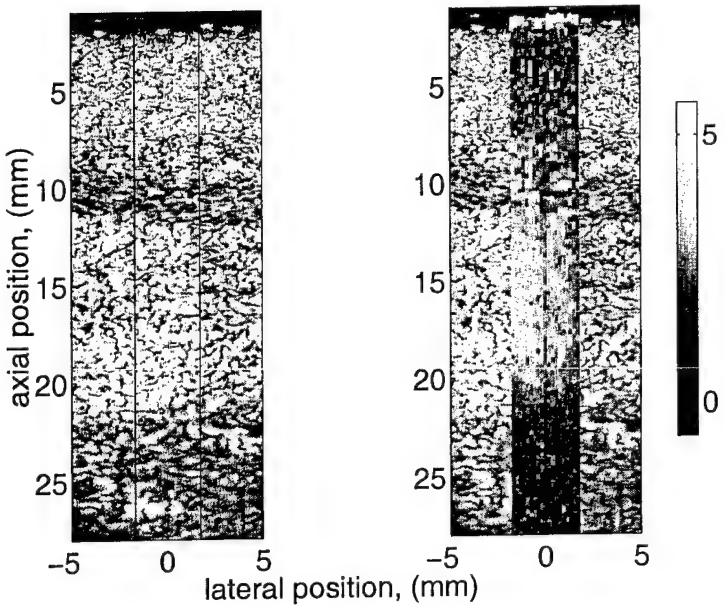


a

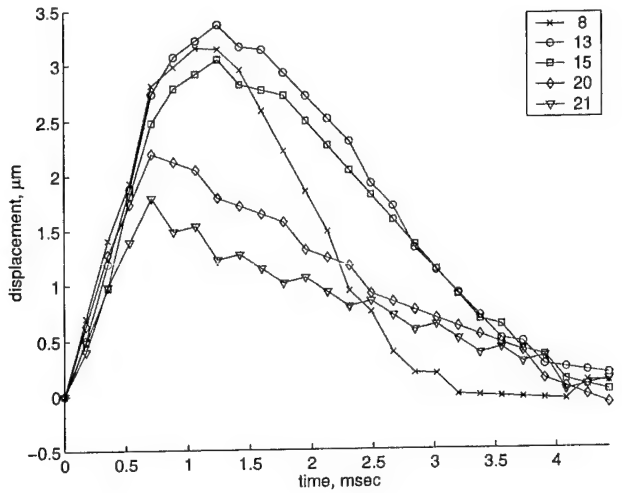


b

Fig. 3.

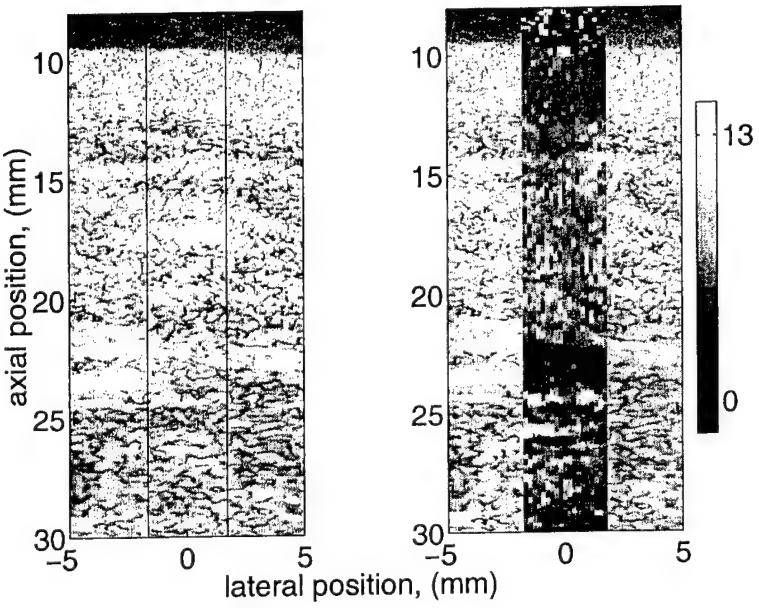


a

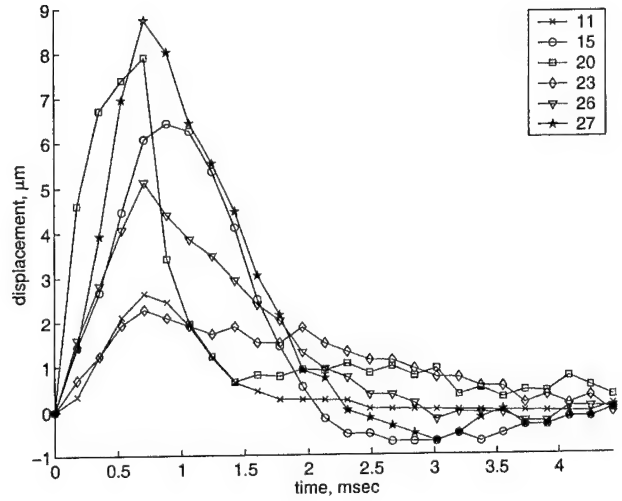


b

Fig. 4.

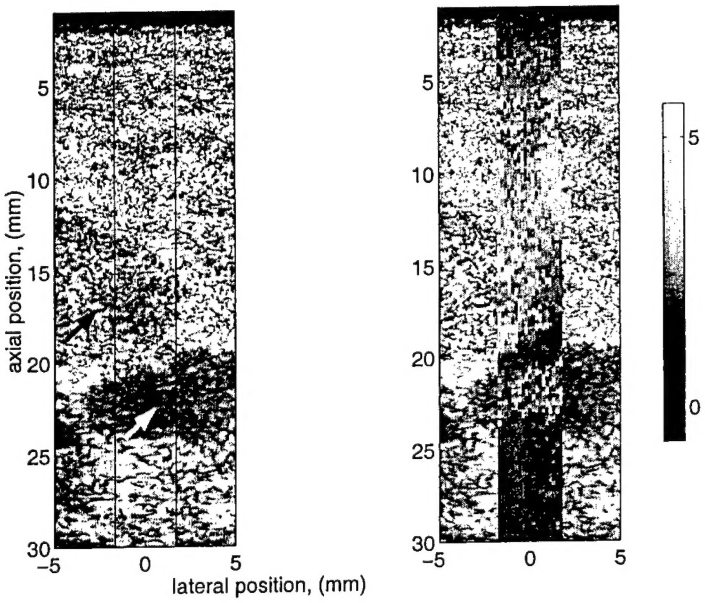
axial position, (mm)
lateral position, (mm)
5
10
15
20
25
30
−5
0
5
5
0

a

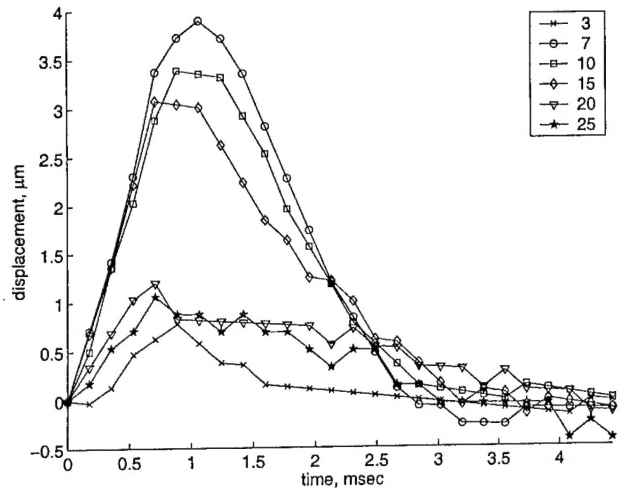
displacement, µm
time, msec
3
7
10
15
20
25
4
3.5
3
2.5
2
1.5
1
0.5
0
−0.5
0
0.5
1
1.5
2
2.5
3
3.5
4

b

Fig. 5.

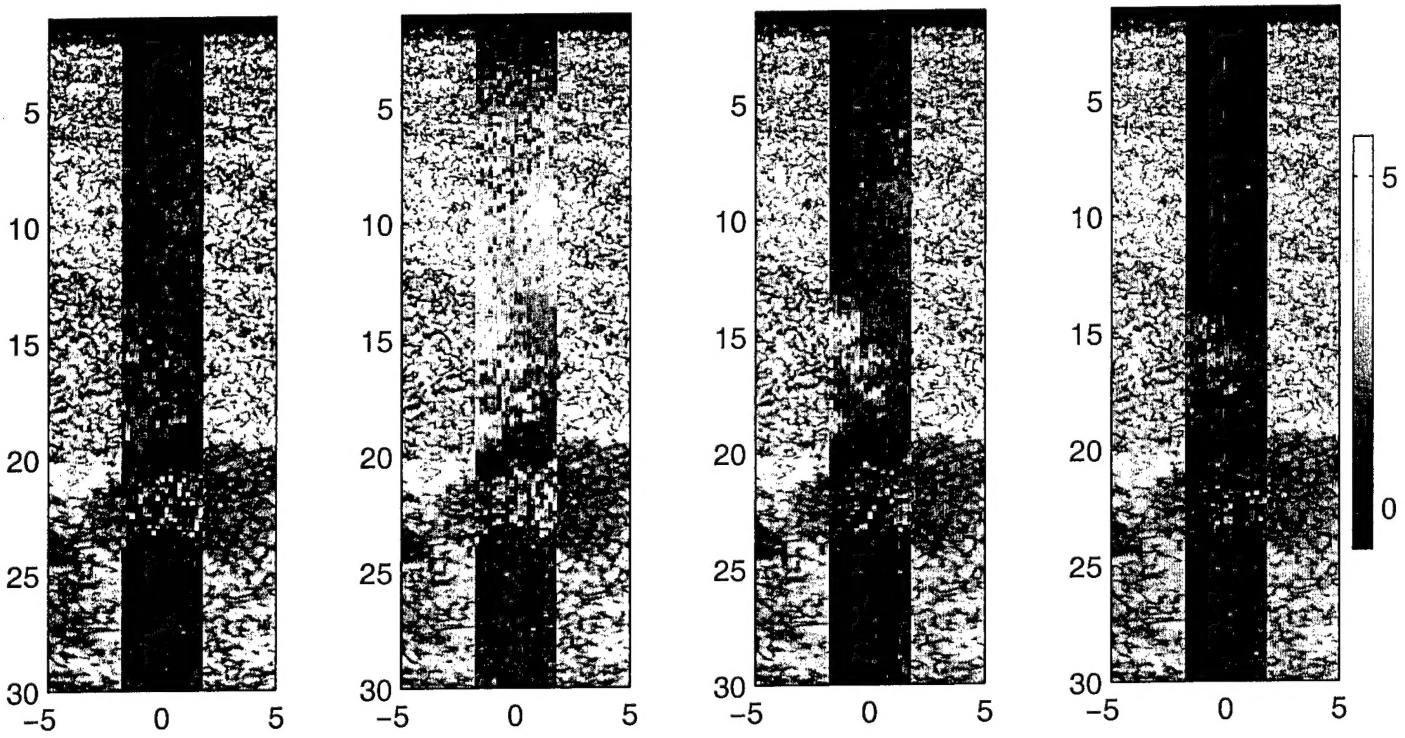


Fig. 6.

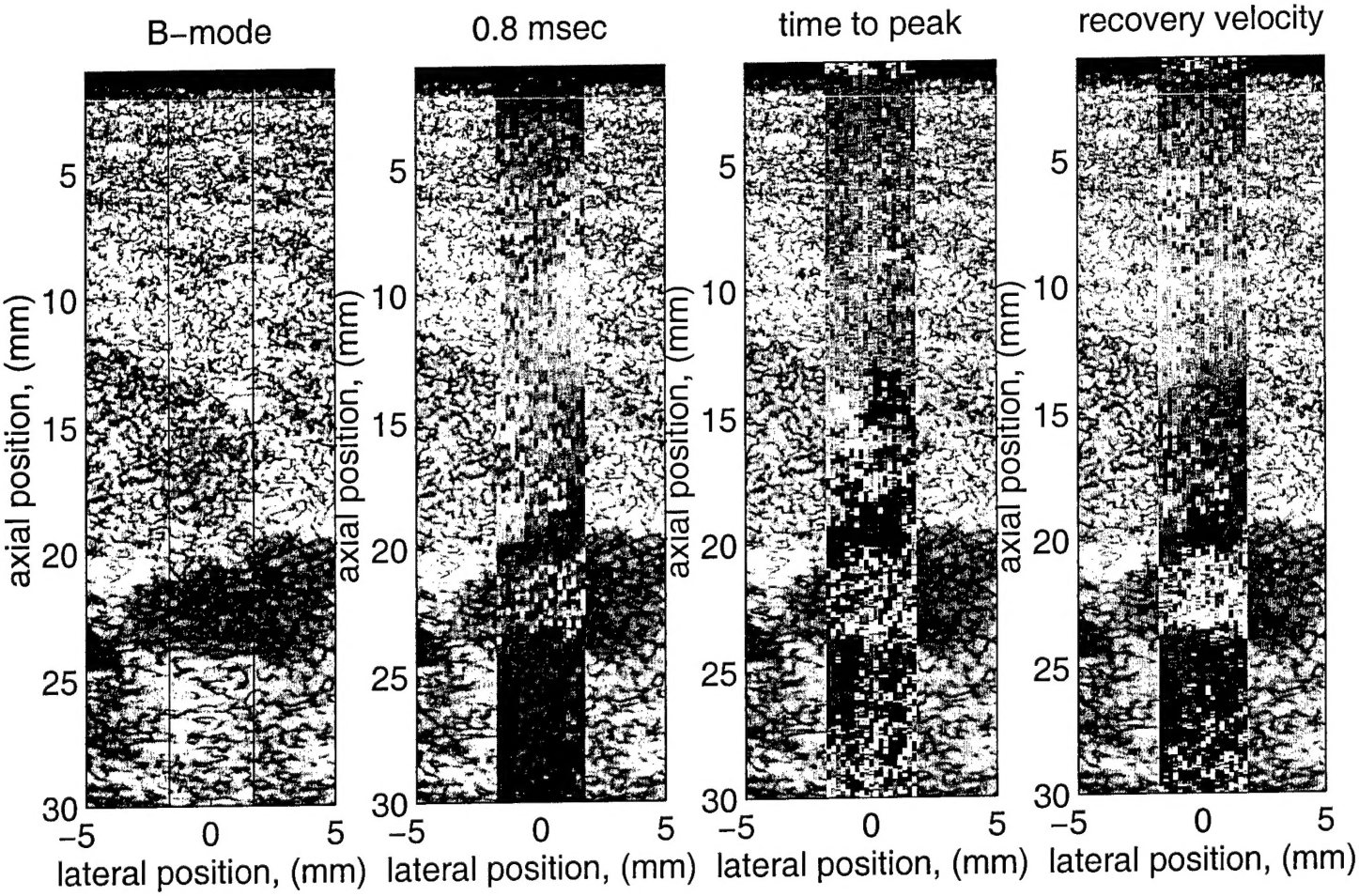
B–mode
0.8 msec
time to peak
recovery velocity
axial position, (mm)
5
10
15
20
25
30
−5
0
5
lateral position, (mm)

Fig. 7.

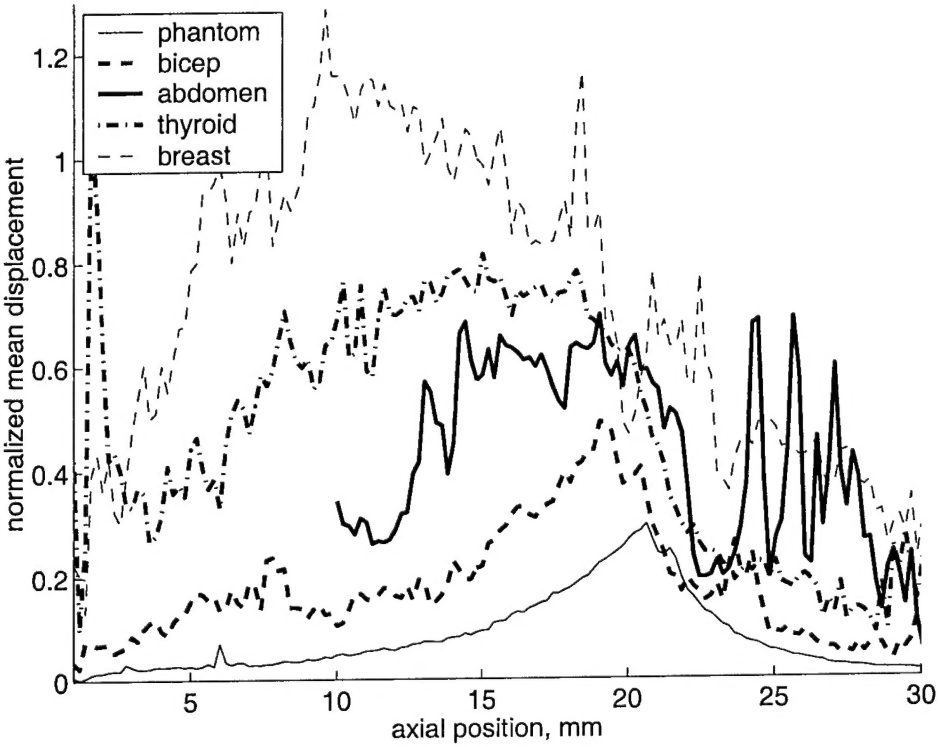
phantom
bicep
abdomen
thyroid
breast
normalized mean displacement
axial position, mm
0
0.2
0.4
0.6
0.8
1
1.2
5
10
15
20
25
30

Fig. 8.